


**RESEARCH ARTICLE**

10.1029/2022MS003328

**Key Points:**

- Recent changes to the Predicted Particle Properties (P3) microphysics scheme combine triple-moment ice with a predicted liquid fraction of mixed-phase hydrometeors
- For a simulated squall line, the changes to P3 reduce the ice accumulation at the surface and increase the cold pool strength and speed
- The simulated reflectivity structure, including the bright band, improves with the new configurations

**Supporting Information:**

Supporting Information may be found in the online version of this article.

**Correspondence to:**

M. Cholette,  
[melissa.cholette@ec.gc.ca](mailto:melissa.cholette@ec.gc.ca)

**Citation:**

Cholette, M., Milbrandt, J. A., Morrison, H., Paquin-Ricard, D., & Jacques, D. (2023). Combining triple-moment ice with prognostic liquid fraction in the P3 microphysics scheme: Impacts on a simulated squall line. *Journal of Advances in Modeling Earth Systems*, 15, e2022MS003328. <https://doi.org/10.1029/2022MS003328>

Received 26 JUL 2022

Accepted 11 MAR 2023

## Combining Triple-Moment Ice With Prognostic Liquid Fraction in the P3 Microphysics Scheme: Impacts on a Simulated Squall Line

Mélissa Cholette<sup>1</sup> , Jason A. Milbrandt<sup>1</sup>, Hugh Morrison<sup>2</sup> , Danahé Paquin-Ricard<sup>1</sup> , and Dominik Jacques<sup>1</sup>

<sup>1</sup>Meteorological Research Division, Environment and Climate Change Canada, Dorval, QC, Canada, <sup>2</sup>National Center for Atmospheric Research, Boulder, CO, USA

**Abstract** The Predicted Particle Properties (P3) bulk microphysics scheme has been recently modified to combine the two major innovations. The triple-moment approach to represent ice, allowing for a freely evolving spectral dispersion of the size distribution, is combined with the predicted liquid fraction, which enables an explicit representation of mixed-phase particles. The impacts of this combination are examined in the context of high-resolution (1-km horizontal grid spacing) simulations of an observed mid-latitude squall line using the Global Environmental Multiscale atmospheric model. The simulation of mixed-phase particles results in a faster squall line propagation speed and stronger cold pool due to greater cooling from the microphysical processes of sublimation, melting and evaporation. There is a reduction in the mass of ice reaching the surface resulting from a decrease in the mean size of melting ice particles aloft with the predicted liquid fraction. Compared to the original double-moment configuration, triple-moment P3 configuration results in larger mean ice sizes at the surface. The reflectivity structure is improved with the new version, now with a more pronounced bright band in the melting zone with the predicted liquid fraction.

**Plain Language Summary** This article describes two major upgrades to a cloud microphysics scheme, which is a component of an atmospheric model that simulates the effects of cloud and precipitation processes. The first change allows for a more flexible representation of ice particles sizes; the second enables the representation of mixed-phase (ice plus water) particles. The impacts of these changes are examined in the context of numerical simulations of a real-case summer convective storm (squall line) using a weather prediction model. The modified cloud scheme results in faster movement of the model storm due to changes to in-cloud microphysical processes, which affect the local air movement. There is also a reduction of ice amounts reaching the surface due to a decrease in the mean ice particle size. The model radar reflectivity structure is notably improved, in particular in the region of melting ice.

### 1. Introduction

Bulk microphysics schemes (BMSs) play a key role in atmospheric models, both for research and for operational numerical weather (NWP). BMSs parameterize cloud and precipitation processes in models. Over the past decades, BMSs have advanced considerably (e.g., Morrison et al., 2020) including those used in large scale NWP and climate models (e.g., Guo et al., 2021; Jouan et al., 2020; Pi & Chen, 2021; Wang et al., 2021). Bulk schemes are becoming more detailed in terms of the microphysical processes that are parameterized. Double-moment BMSs are now widely used operationally (e.g., Benjamin et al., 2016; Milbrandt et al., 2016; Vié et al., 2016) and triple-moment schemes are moving to the forefront (e.g., Luo et al., 2018; Mansell et al., 2020; Milbrandt et al., 2021; Tsai & Chen, 2020 [hereafter M21]), increasing the flexibility in representing hydrometeor size distributions and computing microphysical process rates. One recent conceptual improvement in microphysics parameterization is the property-based approach to represent the continuum evolution of ice-phase hydrometeors, removing the use of pre-defined categories and the need for the artificial conversion processes between them (Hashino & Tripoli, 2007; Jensen et al., 2017; Morrison & Milbrandt, 2015 [hereafter MM15]).

Despite these advances, almost all current BMS still lack the capacity to represent mixed-phase hydrometeors explicitly (Cholette et al., 2019 [hereafter C19]). This lack of mixed-phase particle representation is a notable deficiency in parameterizing several important microphysical processes such as melting, refreezing and wet growth (Frick et al., 2013; C19). As shown by many observational studies (e.g., Rasmussen & Pruppacher, 1982;

Rasmussen et al., 1984a, 1984b; Fujiyoshi, 1986; Hindmarsh et al., 2003; Korolev et al., 2017; Nagumo et al., 2019), these microphysical processes are involved in the formation of several precipitation types that can be associated with high-impact weather (e.g., freezing rain, wet snow, ice pellets and hail). In nearly all state-of-the-art BMSs, including relatively complex schemes, these processes are simplified or ignored. For instance, the melted portion of ice is usually instantly transformed directly into rain instead of accumulating to form denser and smaller mixed-phase particles during the process (Fujiyoshi, 1986). For the melting of unrimed or lightly rimed ice crystals, this can lead to a sharp increase in the hydrometeor fall speed and hence an increase in particle size (e.g., Dawson et al., 2014). The refreezing process is often entirely neglected (Frick et al., 2013) and wet growth (Musil, 1970) results in complete shedding of all liquid instead of forming mixed-phase particles (e.g., Phillips et al., 2014).

The simulation of mixed-phase particles and the tracking of their physical properties is important to compute various important diagnostic fields, both at the surface and aloft, including radar reflectivity (Fabry & Szyrmer, 1999; Fabry & Zawadzki, 1995; Tobin & Kumjian, 2017) and precipitation type (Cholette et al., 2020; Reeves et al., 2016; C19; Thompson, 2019; Xu et al., 2019). For example, a reduction of freezing rain and an increase in ice pellets at the surface was found in the simulations of a high-impact freezing rain event as a result of partial melting and refreezing of mixed-phase particles (Cholette et al., 2020). Since these processes are poorly represented in most BMSs, NWP models often use diagnostic algorithms based on humidity and temperature profiles or diagnose the liquid to solid ratio to forecast surface precipitation types (e.g., Bourgouin, 2000; Forbes et al., 2014; Gascón et al., 2018; Ikeda et al., 2017; Kringlebotn Nygaard et al., 2013; Milbrandt et al., 2012, 2016). Only a few microphysics parameterization schemes, bin or bulk, explicitly predict mixed-phase particles or the liquid water fraction (e.g., Ferrier, 1994; Frick et al., 2013; Loftus et al., 2014; Reeves et al., 2016; C19; Walko et al., 2000).

The production of mixed-phase particles during melting is also responsible for the large increase in reflectivity, commonly referred to as the “bright band,” which coincides with the melting region (e.g., Fabry & Zawadzki, 1995). The bright band is a consequence of the change in the physical properties of ice crystals while undergoing melting (e.g., Fabry, 2015; Houze, 2018). In general, ice crystals composed of only solid ice are characterized by smaller reflectivity than liquid-phase particles. As ice crystals fall into warm atmospheric layers ( $T > 0^{\circ}\text{C}$ ), melting starts and mixed-phase particles are formed, composed of both solid and liquid. Therefore, due to the liquid surrounding the ice core, the particles start to look like large raindrops which changes the backscattering properties and leads to an increase in reflectivity. As melting continues, particles' sizes decrease and raindrops are produced at the complete stage of melting. During this process, particles start to fall faster which reduces the number of hydrometeors per unit volume leading to a decrease in reflectivity. As radars are widely used to detect high-impact convective weather, their data are directly compared with model-diagnosed reflectivity to evaluate forecasts (Jacques & Michelson, 2022; Jacques et al., 2018; Ryzhkov et al., 2020; Wang et al., 2011). In NWP models, for bulk schemes that do not predict the liquid fraction, the reflectivity maxima associated with the melting layer can be simulated by diagnosing the liquid fraction. However, this is often neglected for simplicity. For several schemes in the Weather and Research Forecasting model (WRF; Skamarock & Klemp, 2008), reflectivity in the melting region is diagnosed by estimating the liquid fraction of melting ice, snow and graupel as  $(1 - q_x)/q_{x,k\_above\_0}$ , where  $q_x$  is the mass mixing ratio (all symbols and units are in Appendix A) and  $q_{x,k\_above\_0}$  is the mixing ratio at the level just above the  $0^{\circ}\text{C}$  level. Here  $x$  may be i, s or g for the melting of ice, snow or graupel, respectively (Blahak, 2016; Wolfensberger & Berne, 2018).

The Predicted Particle Properties (P3) scheme was introduced as a property-based BMS in MM15. P3 has been used for several research studies by various groups (e.g., Dietlicher et al., 2018; Johnson et al., 2019; C19; Jouan et al., 2020; M21; Paukert et al., 2019; Wang et al., 2021). P3 is also used operationally in the Environment and Climate Change Canada's high-resolution (2.5- km horizontal grid spacing) NWP system (HRDPS; Milbrandt et al., 2016, 2018) and is available in the public release of WRF. Since its original inception in 2015, there have been several major independent developments to P3 (see Appendix B), including the prediction of the bulk liquid mass fraction of mixed-phase particles (C19) and the 3-moment treatment of ice (M21). The 3-moment ice parameterization itself has impacts on the simulation of convective meteorology and the diagnosed radar reflectivity structure. M21 identified that the 3-moment ice microphysics in P3 leads to an improved capacity to simulate large, heavily rimed ice (hail) in a supercell for which P3 had previously been identified as being deficient (Johnson et al., 2019).

To date, the combined effects of the 3-moment treatment of ice with the predicted liquid fraction have not been examined in any microphysics scheme (to our knowledge), nor have the effects of the predicted liquid fraction in P3 on simulations of deep convection been studied. This paper describes the latest version of P3, which now combines 3-moment ice with the parameterization of the bulk liquid fraction of mixed-phase particles. The new version is tested in the context of mesoscale model simulation, with a 1-km horizontal grid spacing, of a mid-latitude squall line and is compared to simulations with simpler configurations of P3, including with 2-moment ice, with and without mixed-phase particles, and 3-moment ice without mixed-phase particles. Numerical simulations of a squall line help to identify the impacts of microphysics on storm dynamics, development and persistence, while allowing to study the impacts of parameterization on both the convective and the stratiform parts of the precipitation simultaneously (e.g., Adams-Selin et al., 2013a, 2013b; Bao et al., 2019; Cao et al., 2022; Han et al., 2019; Jensen et al., 2018; Li et al., 2021; Liu et al., 1997; Morrison et al., 2009, 2015; Wen et al., 2017; Wu et al., 2013; Zhao et al., 2021). This study examines how explicitly representing mixed-phase particles impacts melting, sublimation, and evaporation, since these processes are critical for generating cold pools that drive the propagation of squall lines (e.g., Dawson et al., 2010; Houze, 2018; Tao et al., 1995).

The remainder of the paper is organized as follows. Section 2 gives a description of the modified P3 scheme combining 3-moment ice with the prediction of the bulk liquid fraction, including a description of an improved calculation of equivalent reflectivity. Section 3 describes the simulation configurations and the analysis methodology. The squall line case and coarser resolution (approximately 2.5 km horizontal grid spacing) results are presented in Section 4. In Section 5, impacts of the combined 3-moment ice and predicted liquid fraction in finer resolution simulations (approximately 1 km grid spacing) are analyzed. Section 6 provides a summary and conclusions.

## 2. The Modified P3 Scheme

### 2.1. Prognostic Variables and Particle Size Distribution

The evolution of the P3 scheme and a detailed description of the baseline configuration used in this study is summarized in Appendix A. The prognostic variables and microphysical processes associated with the liquid-phase categories are common to all configurations of P3. This section focuses on the ice-phase description of the new P3 version. Each ice category in P3 (the single category is used in this study) has up to 6 prognostic variables:  $N_{i,\text{tot}}$ ,  $q_{i,\text{tot}}$ ,  $q_{i,\text{liq}}$ ,  $q_{i,\text{rim}}$ ,  $B_{i,\text{rim}}$  and  $Z_{i,\text{tot}}$  (Appendix A), two of which are optional ( $q_{i,\text{liq}}$  and  $Z_{i,\text{tot}}$ ).  $q_{i,\text{liq}}$  is the mixing ratio of liquid mass on ice for mixed-phase particles (C19) and  $Z_{i,\text{tot}}$  is the mixing ratio of the 6th moment of the particle size distribution for the 3-moment treatment of ice (M21).

The mass mixing ratio of ice- and mixed-phase particles ( $q_{i,\text{tot}}$ ) is computed as

$$q_{i,\text{tot}} = q_{i,\text{dep}} + q_{i,\text{rim}} + q_{i,\text{liq}} = q_{i,\text{ice}} + q_{i,\text{liq}} \quad (1)$$

where  $q_{i,\text{dep}}$  is the mixing ratio of ice mass from vapor diffusion,  $q_{i,\text{rim}}$  is the rimed ice mass mixing ratio, and  $q_{i,\text{ice}}$  is the total ice mass mixing ratio. Several bulk properties are predicted including the bulk rime mass fraction  $F_{i,\text{rim}} = q_{i,\text{rim}}/q_{i,\text{ice}}$ , the bulk rime density  $\rho_{i,\text{rim}} = q_{i,\text{rim}}/B_{i,\text{rim}}$  (where  $B_{i,\text{rim}}$  is the volume rimed mixing ratio) and the bulk liquid mass fraction of mixed-phase particles  $F_{i,\text{liq}} = q_{i,\text{liq}}/q_{i,\text{tot}}$ . Note that if the predicted liquid fraction is not used, the scheme reverts to either the 2-moment or the 3-moment configurations without liquid fraction and will give the same solution as version 4 (see Appendix B).

Prognostic variables  $q_{i,\text{tot}}$  and  $N_{i,\text{tot}}$  (the total ice number mixing ratio) are proportional to moments of (i.e., integrals over) the particle size distribution ( $N(D)$ ; Equation 2) and mass-diameter relationship ( $m(D)$ ; Equation B4) for  $q_{i,\text{tot}}$ . The size distribution is represented by a gamma function:

$$N(D) = N_0 D^\mu \exp(-\lambda D) \quad (2)$$

where  $D$  is the equivalent-volume diameter (In MM15,  $D$  was defined as the “maximum dimension.” This was slightly incorrect since, for unrimed and partially rimed ice, the  $m$ - $D$  parameters are based on measurements from Brown and Francis (1995) who defined  $D$  as the mean of the maximum observed crystal dimensions in the horizontal and vertical. This is equivalent to the estimated diameter of a sphere of equivalent volume to that of an ellipsoid encapsulating the particle.) of the ice particle,  $\mu$  is the spectral shape parameter, and  $N_0$  [ $\text{kg}^{-1} \text{m}^{-(1+\mu)}$ ] and  $\lambda$  [ $\text{m}^{-1}$ ] are the intercept and slope parameters, respectively. All integrations over the size distribution to

compute microphysical process rates are made off-line and stored in lookup tables as a function of numerous values of  $q_{i,\text{tot}}/N_{i,\text{tot}}$ ,  $F_{i,\text{rim}}$ ,  $\rho_{i,\text{rim}}$ ,  $F_{i,\text{liq}}$  (for the optional predicted liquid fraction) and  $\mu$  (for the optional 3-moment ice). Values of  $\mu$  specified for the 2-moment treatment of ice with and without the predicted  $F_{i,\text{liq}}$  are described in Appendix B (Equation B3) and follow MM15, C19 and M21. For the 2-moment configurations,  $\mu$  is a function of the slope parameter  $\lambda$ , the rime mass fraction  $F_{i,\text{rim}}$  and the mass-weighted mean ice particle density  $\rho_m$ ; the latter is also a function of  $F_{i,\text{liq}}$  for the 2-moment P3 with predicted liquid fraction.

## 2.2. Combining Triple-Moment Ice With the Predicted Liquid Fraction

For the 3-moment ice configuration of P3,  $\mu$  varies as a free parameter in time and space as a function of the prognostic variables of the size distribution:  $N_{i,\text{tot}}$ ,  $q_{i,\text{tot}}$  and  $Z_{i,\text{tot}}$  (Appendix B; Equation B5). Some closure assumptions are needed to derive tendencies for  $Z_{i,\text{tot}}$  (Appendix B). Merging the predicted  $F_{i,\text{liq}}$  and the 3-moment ice ( $Z_{i,\text{tot}}$ ) is kept as simple as possible; refinements may be the subject of future work. Process tendencies for  $Z_{i,\text{tot}}$  and closure assumptions for  $\mu$  are computed similarly with and without the predicted  $F_{i,\text{liq}}$ . When  $F_{i,\text{liq}}$  is predicted, most processes (i.e., collection of liquid, wet growth, collision-aggregation, refreezing, shedding and vapor condensation/evaporation) are calculated by integrating over the particle size distribution corresponding to the full particle size (including both liquid and ice portions for mixed-phase particles) and thus use  $N_{i,\text{tot}}$ ,  $q_{i,\text{tot}}$ , and  $Z_{i,\text{tot}}$  to obtain the size distribution parameters required for integration (Appendix B). Other processes are assumed to act on the ice core of mixed-phase particles (i.e., sublimation/deposition and melting). In that case, the integrations are over the “ice core” size distribution, and use  $N_{i,\text{tot}}$  and  $(1 - F_{i,\text{liq}})q_{i,\text{tot}}$  along with, for simplicity,  $\mu$  for the full particle size distribution to obtain the size distribution parameters required for integration. The closure assumption to obtain process tendencies for  $Z_{i,\text{tot}}$  for mixed-phase particles ( $0 < F_{i,\text{liq}} < 1$ ) with the 3-moment treatment of ice is that  $\mu$  is constant during the time step because its change is assumed to be small compared to tendency from sedimentation. Calculation of the two other size distribution parameters ( $\lambda$  and  $N_0$ ) for both the full particle and ice core size distributions follows C19 and in MM15.

As the predicted liquid fraction has important impacts on the particle size distribution as the liquid fraction changes (Cholette et al., 2020), the closure assumption for  $\mu$  for the processes that directly affect the mean density could be improved. Since  $dD^6/dt$  can be computed for some of the microphysical processes, such as melting, refreezing and vapor diffusion, the closure assumptions for  $\mu$  during these processes could be modified accordingly. In this way, behavior such as broadening of the size distribution owing to the decrease of diameter during melting would be captured. Such improvements in the closure assumption for  $\mu$  will be explored in further studies both for configurations with and without the predicted liquid fraction.

## 2.3. Calculation of Model Reflectivity

An additional update with respect to the reflectivity calculation for mixed-phase particles is introduced in P3. The baseline calculation of the total equivalent reflectivity of ice is given in Appendix C. The updated reflectivity for  $0 < F_{i,\text{liq}} < 1$ , also given in Appendix C, is based on the approach used in the WRF model, which uses the same equations to compute the reflectivity for many of the available microphysics schemes. Modifications to the approach used in WRF were made for its application to P3, with the main difference being that P3 now explicitly predicts the liquid fraction on mixed-phase particles whereas in WRF the liquid fraction is diagnosed based on the ice/snow/graupele mixing ratio profiles.

# 3. Model Configuration and Analysis

## 3.1. GEM Configuration

Five simulations (listed in Table 1) of a mid-latitude squall line (described in Section 4) were performed with the Global Environmental Multiscale model (GEM; Côté et al., 1998; Girard et al., 2014). GEM is the operational NWP model used in all atmospheric prediction systems of Environment and Climate Change Canada. GEM's dynamical core solves the compressible Euler equations using an implicit treatment in time and a semi-Lagrangian advection scheme (Girard et al., 2014). The version used in this study is nonhydrostatic. The first simulation, with a horizontal grid spacing of approximately 2.5 km, provides the initial and lateral boundary conditions (updated every 1 hr) for the four simulations with 1-km grid spacings that are analyzed in detail. All five simulations use the single-ice-category configuration of P3.

**Table 1**  
*List of Simulations*

Name	Description	Prognostic variables for P3
3MOM_LF_2.5KM	HRDPS configuration at 2.5 km grid spacing, with 3-moment ice and predicted liquid fraction	$N_{i,\text{tot}}$ , $q_{i,\text{tot}}$ , $q_{i,\text{rim}}$ , $B_{i,\text{rim}}$ , $q_{i,\text{liq}}$ , $Z_{i,\text{tot}}$
2MOM_noLF	1 km grid spacing, 2-moment ice	$N_{i,\text{tot}}$ , $q_{i,\text{tot}}$ , $q_{i,\text{rim}}$ , $B_{i,\text{rim}}$
3MOM_noLF	1 km grid spacing, 3-moment ice	$N_{i,\text{tot}}$ , $q_{i,\text{tot}}$ , $q_{i,\text{rim}}$ , $B_{i,\text{rim}}$ , $Z_{i,\text{tot}}$
2MOM_LF	1 km grid spacing, 2-moment ice with predicted liquid fraction	$N_{i,\text{tot}}$ , $q_{i,\text{tot}}$ , $q_{i,\text{rim}}$ , $B_{i,\text{rim}}$ , $q_{i,\text{liq}}$
3MOM_LF	1 km grid spacing, with 3-moment ice and predicted liquid fraction	$N_{i,\text{tot}}$ , $q_{i,\text{tot}}$ , $q_{i,\text{rim}}$ , $B_{i,\text{rim}}$ , $q_{i,\text{liq}}$ , $Z_{i,\text{tot}}$

The 2.5-km simulation configuration is based on the operational HRDPS (Caron et al., 2021; McTaggart-Cowan et al., 2019; Milbrandt et al., 2016). Initial and hourly lateral boundary conditions are from ECCC's operational Regional Deterministic Prediction System (RDPS; Caron et al., 2015; McTaggart-Cowan et al., 2019) forecasts of state variables. Lateral boundary conditions include information about cloud condensate from the grid-scale condensation scheme (Sundqvist et al., 1989). The computational domain is shown in Figure 1; the horizontal grid spacing is  $0.0225^\circ$  ( $\sim 2.5$  km) with 62 staggered vertical levels. The lowest thermodynamic level is at approximately 20 m AGL. Physical parameterizations include the Kain and Fritsch scheme for deep convection (Kain & Fritsch, 1990, 1993) and the Kuo-Transient scheme for shallow convection (Bélair et al., 2005). The land surface scheme is ISBA for the Integrations between Soil, Biosphere, and Atmosphere (Bélair et al., 2003, 2005). The boundary layer turbulent mixing is based on a prognostic turbulent kinetic energy approach (Benoit et al., 1989; Delage, 1988b) with a statistical representation of subgrid-scale clouds (Bélair et al., 2005). No turbulent mixing is applied to the prognostic hydrometeor in this study. The Li-Barker correlated k-distribution method is used to compute radiative transfer every 15 min (Li & Barker, 2005). Latent heat nudging (Jacques et al., 2018; Jacques & Michelson, 2022) during the assimilation period ( $-3$  hr to  $+3$  hr) is employed for this simulation only. Latent heat nudging is a simple assimilation technique where vertical profiles of temperature (and moisture) are adjusted for a better correspondence between the precipitation that is simulated and inferred from radar observations.

The four simulations examined in detail have a grid spacing of  $0.01^\circ$  (approximately 1 km) and are nested within the 2.5-km simulation domain (red box in Figure 1). Models with grid spacings near or below 1 km are typically considered to represent deep convection sufficiently such that a deep convection parameterization scheme is not used (e.g., Li et al., 2015; Luo & Chen, 2015; Weisman et al., 1997). This simplifies the interpretation of the sensitivity tests since all changes in the results can be attributed directly to changes in the microphysics scheme, without the complication of indirect changes on the behavior of the deep convection scheme. Note that at horizontal grid spacing of  $\sim 2.5$  km a deep convection scheme is often not used. However, the simulation of deep convection is improved in GEM at this resolution with the Kain-Fritsch convection scheme activated (Milbrandt et al., 2016), and therefore it is used in the operational HRDPS as well as in the 2.5-km simulation in this study. The 2.5-km “driving model” simulation uses the new P3 configuration, with 3-moment ice and mixed-phase particles (i.e., prognostic  $q_{i,\text{liq}}$ ); this run is hereafter referred to as 3MOM\_LF\_2.5KM.

The 1-km simulations include P3 with the predicted  $F_{i,\text{liq}}$  of mixed-phase particles for both the 2- and 3-moment configurations (2MOM\_LF, 3MOM\_LF, respectively; LF is for liquid fraction) and without the predicted  $F_{i,\text{liq}}$  again for both the 2- and the 3-moment configurations (2MOM\_noLF, 3MOM\_noLF, respectively). The differences between 3MOM\_LF\_2.5KM and the 1-km simulations, apart from the grid spacing, are the simulation period, the time step, and exclusion of the deep convection scheme at 1 km. The simulated period is 12 hr for the 2.5-km simulation (from 00 UTC to 12 UTC 18 August 2019) and 9 hr for the 1-km simulations (from 03 UTC to 12 UTC). The time steps are 60 and 30 s for the 2.5-km and the 1-km simulations, respectively. All simulation outputs are saved every 1 hr. Also, the latent heat nudging is only used for the 3MOM\_LF\_2.5KM and not for the 1-km simulations.

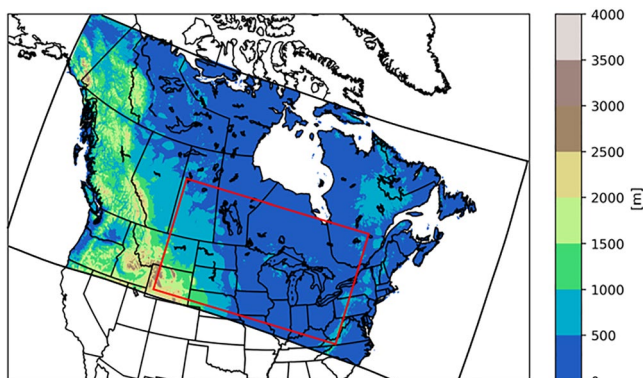


**Figure 1.** Elevations [m] of the 3MOM\_LF\_2.5KM simulation and the location of the domain for the four 1-km simulations (red box).

### 3.2. Analysis

The simulated reflectivity structure is compared to the BALTRAD radar mosaic (Michelson et al., 2018) and with KARX and KDVN radars. The total precipitation accumulation is compared against the StageIV precipitation analysis at 4-km resolution (Du, 2011) and the Multi-Radar Multi-Sensor at 1-km resolution (MRMS; Zhang et al., 2011).

Since the cold pool is mainly driven by melting and rain evaporation, the cold pool parameters are investigated to study the impacts of mixed-phase particles on microphysical processes. The methods to compute the cold pool speed vary between studies (e.g., Bryan et al., 2006; Fan et al., 2017; Jouan & Milbrandt, 2019; Morrison et al., 2015; Zhao et al., 2021). Many previous studies, including with real cases, compute the cold pool properties over some region where the perturbation of potential temperature is less than  $-1$  or  $-2$  K or over a selected small region behind the gust front. This can lead to difficulties when comparing simulations between one another because it is hard to define the base state for the mean potential temperature in real cases like the current one. Instead, we define the cold pool region based on the simulated reflectivity near 1-km height (AGL) over an analysis domain smaller than the simulation domain. This analysis domain is  $522 \times 522$  grid points and covers the state of Iowa. The idealized cold pool speed ( $C$ ; Equation 3) is computed for each hour between 05 and 10 UTC and spatially averaged over the small domain where the simulated reflectivity ( $Z_e$ ) at 1-km height is  $>40$  dBZ:

$$C^2 = 2 \int_0^H -B dz = \int_0^H -2g \left[ \frac{\theta - \bar{\theta}}{\bar{\theta}} + 0.61(q_v - \bar{q}_v) - q_c - q_r - q_{i,tot} \right] dz \quad (3)$$

where  $H$  is the height of the cold pool, limited by either  $B < 0$  or  $H < 5$  km and  $T < 0^\circ\text{C}$ ,  $B$  is the buoyancy,  $g$  the gravitational acceleration,  $\theta$  the potential temperature, and  $q_v$ ,  $q_c$ , and  $q_r$  are the mass mixing ratios of water vapor, cloud and rain, respectively.  $\bar{\theta}$  and  $\bar{q}_v$  are the spatial means of potential temperature and water vapor mixing ratio, respectively, over the analysis domain. The mean perturbation potential temperature ( $\theta' = \theta - \bar{\theta}$ ), the mean depth of the cool pool  $\bar{H}$  as well as the total mean latent cooling over the cold pool region from the simulations will be also discussed in this analysis. The total cooling from the microphysics is the sum of ice sublimation, melting, mixed-phase particle evaporation, rain evaporation and cloud evaporation computed over the cold pool region.

## 4. The Squall Line Case and the 3MOM\_LF\_2.5KM Simulation

The squall line case occurred between 03 and 12 UTC 18 August 2019 in Iowa, in the central U.S. This case is selected because it was well reproduced in terms of timing, location, and structure by the operational HRDPS at the time it was forecasted. A low surface pressure of around 996 hPa, as well as a low in the 500 hPa geopotential height, at the border between Saskatchewan and Manitoba, Canada was quasi-stationary over the entire 12-hr period (Figure 2 at 06 UTC). Surface air temperatures in Iowa were between  $25^\circ\text{C}$  and  $30^\circ\text{C}$  at around 00 UTC 18 August but dropped to between  $15^\circ\text{C}$  and  $20^\circ\text{C}$  at 12 UTC (not shown). Surface winds in Iowa were southerly over the entire period to the east of the squall line's gust front.

Observed atmospheric soundings at 00 UTC show convective available potential energy (CAPE) values of  $2,930 \text{ J kg}^{-1}$  and  $1,035 \text{ J kg}^{-1}$  at OAX and DVN, respectively (Figure 3). Winds at higher levels (above 700 hPa) were generally westerly at both stations. Initial profiles from the 3MOM\_LF\_2.5KM simulation are also shown in Figure 3. At OAX, the simulated winds at lower levels are shifted slightly south compared to observations and temperatures are lower between 800 and 900 hPa. At DVN, the initial vertical profile of temperature is very similar to observations, which is expected since this sounding was assimilated into the analysis used for the initial conditions. Soundings at 12 UTC are discussed in Section 5 for the 1-km simulations results.

The observed squall line developed a trailing stratiform structure (Parker & Johnson, 2000) as seen by hourly evolution of the low-level reflectivity (Figure 4). At 04 UTC, the squall line was near the border between South Dakota, Minnesota and Iowa. Between 05 and 08 UTC, it moved into the northern portion of Iowa. At the mature stage, at 08, 09, and 10 UTC, the convective line was oriented west-to-east across Iowa with a length of approximately 630 km. The squall line began to dissipate at 11 UTC and the active deep convection was almost gone by 12 UTC (not shown). In the early stages of the squall line, stratiform precipitation was mainly associated with a mesoscale convective vortex (MCV) located near the northern end of the squall line, but trailing stratiform precipitation later developed parallel to the squall line as the line moved away and became separated from the MCV.

## Synoptic conditions at 06 UTC 18 Aug 2019

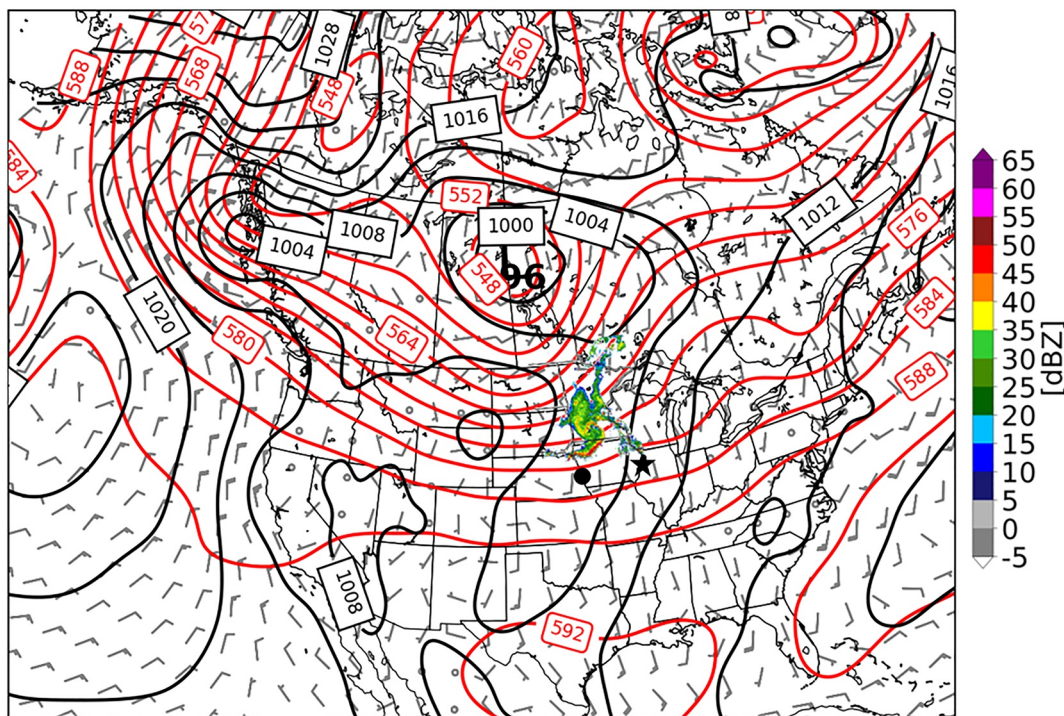


**Figure 2.** Mean sea-level pressure (black; every 4 hPa), geopotential height at 500 hPa (red; every 4 dam), 10-m horizontal wind barbs (knots) from ERA5 reanalysis (Hersbach et al., 2020) with flags, pennants, and half-pennants denoting 50, 10, and 5 knots, respectively. The observed radar reflectivity at 06 UTC 18 August 2019 (colors; cropped from Figure 4b; every 5 dBZ) shows the location of the squall line. Also shown are the locations of the DVN (black star) and OAX (black dot) meteorological stations.

The spatial extent, location, and intensity of the simulated squall line in 3MOM\_LF\_2.5KM compare reasonably well with the BALTRAD radar observations. However, the 3MOM\_LF\_2.5KM results (Figure 5) have higher reflectivity near 1-km height in both the leading convective region of the squall line and the trailing stratiform region of the later stages. The squall line orientation and length are well reproduced by the simulation, but there is not enough bowing at the mature stage in the simulation. The simulated squall line also moves somewhat faster than the observed storm. The spatial extent of reflectivity higher than 45 dBZ is larger in the simulation than observed, particularly at the mature stage, but decreases substantially in the 1-km simulations (shown later in Section 5). The 1-km simulations also produce a more bowed line structure with a closer resemblance to the observed squall line.

## 5. Analysis of the 1-km Simulations

### 5.1. Temperature and Precipitation

Time-mean differences in the lowest model level temperature among the 1-km simulations are shown in Figure 6. For P3 configurations both with and without the predicted liquid fraction (LF and noLF, respectively), the temperature is in general higher after the passage of the squall line with the 3MOM compared to the 2MOM configuration, but with considerable spatial variability (Figures 6a and 6b). A similar but smaller warming is obtained in the comparison between LF and noLF (Figures 6c and 6d) after the passage of the storm. An overall lower temperature is obtained using LF compared to noLF in the cold pool region for both 2MOM and 3MOM. The large temperature differences in Iowa are caused by changes in the location of the gust front from the hourly output data. Temporally-averaged vertical profiles of temperature in regions with simulated reflectivity at 1-km height higher than 40 dBZ are similar between the four runs, although the LF simulations are colder by about 1–1.5°C below 4 km (not shown). 2MOM\_noLF is relatively warmer at these heights. Consistent with the

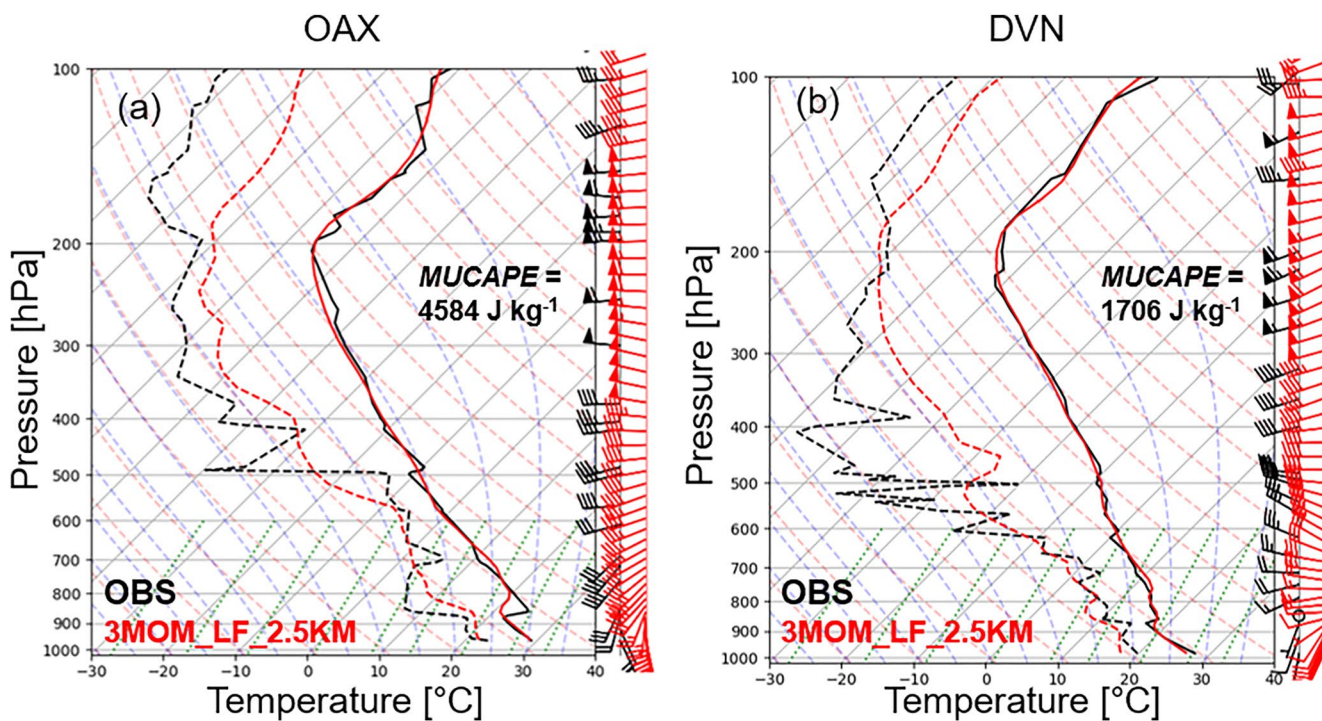


**Figure 3.** Soundings at 00 UTC 18 August 2019 from (a) OAX and (b) DVN for the observations (black) and the 3MOM\_LF\_2.5KM simulation (red). Solid lines are temperature [ $^{\circ}\text{C}$ ], dashed lines are dew point temperature [ $^{\circ}\text{C}$ ] and the wind barbs are in knots, with flags, pennants, and half-pennants denoting 50, 10, and 5 knots, respectively. The most unstable CAPE (MUCAPE) from the observed sounding is indicated in each panel. 3MOM\_LF\_2.5KM MUCAPE values are  $3,921 \text{ J kg}^{-1}$  and  $475 \text{ J kg}^{-1}$  at OAX and DVN, respectively.

stronger cold pools (see Section 5.2), squall lines in the LF simulations move faster compared to noLF for both the 2MOM and the 3MOM configurations (Figures 6c and 6d). For both 2MOM and the 3MOM, the gust front moves  $\sim 4 \text{ km hr}^{-1}$  faster with LF compared to noLF. The 3MOM gust front speed is in general also faster by  $1 \text{ km hr}^{-1}$  compared to 2MOM.

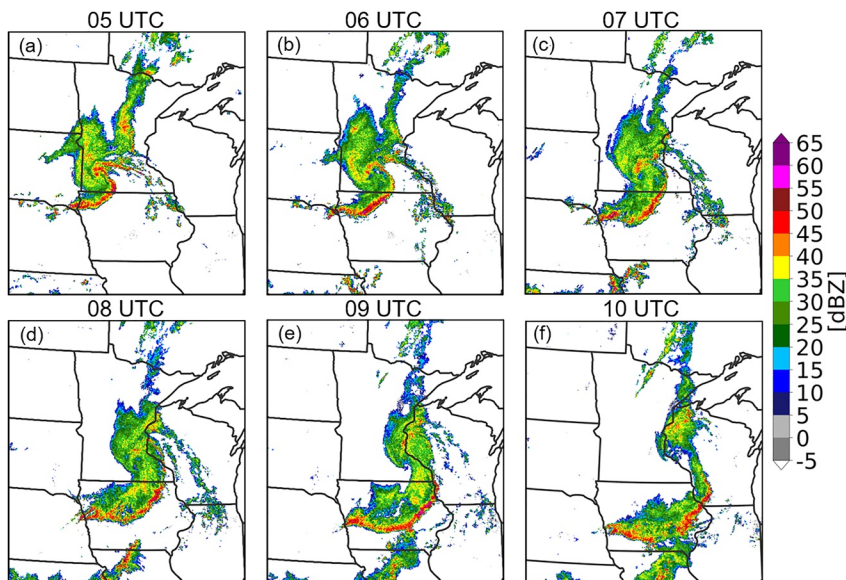


**Figure 4.** Hourly evolution from 05 UTC to 10 UTC 18 August 2019 of BALTRAD pseudo-CAPPIs of radar reflectivity at 1-km height ( $Z$ , [dBZ]; Michelson et al., 2018).

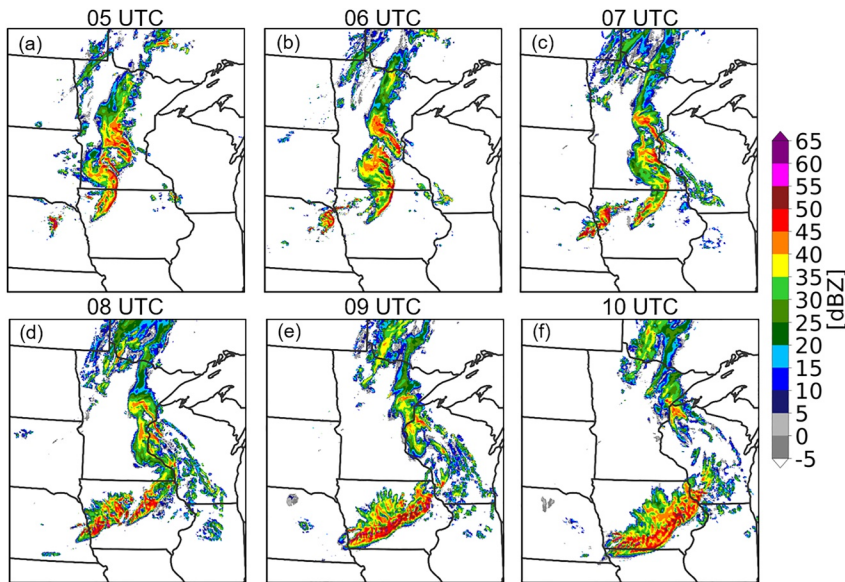


**Figure 5.** Hourly evolution from 05 UTC to 10 UTC 18 August 2019 of equivalent reflectivity ( $Z_e$ , [dBZ]) in 3MOM\_LF\_2.5KM at the model level closest to 1-km height.

The 1-km simulations all closely reproduce the observed vertical profile of temperatures at DVN at 12 UTC 18 August 2019 but have lower dew point temperatures at levels below 700 hPa (Figures 7b and 7d). At OAX (Figures 7a and 7c), all simulated temperatures are higher between 700 and 800 hPa and lower below 800 hPa compared to observed but with a better comparison of the dew point temperatures at these levels compared to at DVN. Differences with and without LF are small, except at lower levels for DVN where LF is warmer at levels below 950 hPa and colder between 950 and 600 hPa for both 2MOM and 3MOM. Surface air temperatures are similar between the four runs at both stations, but slightly higher at DVN and slightly lower at OAX (by about 1°C) for LF compared to noLF for both 2MOM and 3MOM. At levels between 850 and 950 hPa, only 2MOM\_noLF shows higher temperature at DVN compared to the three other simulations that are slightly colder and overall closer to the observed sounding. All simulations miss the observed weak easterly winds at low levels at OAX, but the observed wind speed and direction are overall well reproduced at higher altitudes at OAX and at all altitudes at DVN.

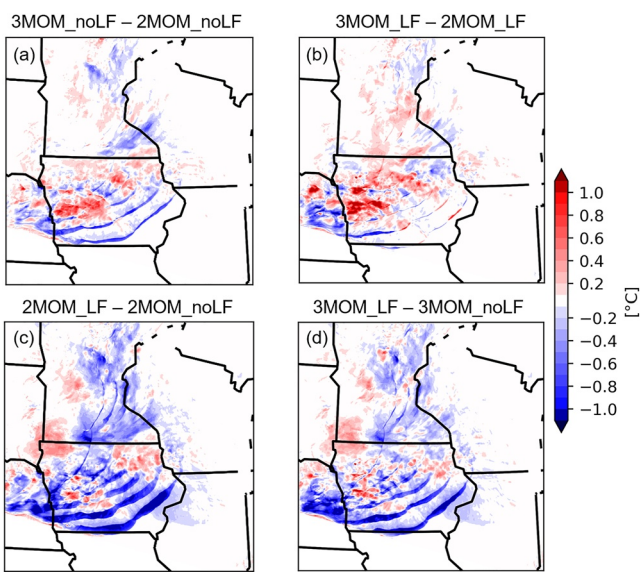


**Figure 6.** Difference in simulated lowest model level temperature averaged between 04 and 10 UTC (using hourly output) for: (a) 3MOM\_noLF–2MOM\_noLF, (b) 3MOM\_LF–2MOM\_LF, (c) 2MOM\_LF–2MOM\_noLF and (d) 3MOM\_LF–3MOM\_noLF.

All simulations, including 3MOM\_LF\_2.5KM, overestimate the total accumulated precipitation compared to StageIV and MRMS (Figure 8) in Iowa, but underestimate it in Minnesota. For both 2MOM and the 3MOM, LF produces much more accumulated precipitation in the southern portion of the domain (Iowa) (Figures 8f and 8i) than noLF. This occurs because the squall lines with LF move faster on average and thus reach further into southern and eastern Iowa by the end of the analysis period compared to the noLF simulations. Kernel density estimate of precipitation rates (Figure 9) show that 2MOM\_noLF has the highest frequency of small precipitation rates ( $< 2 \text{ mm hr}^{-1}$ ), while 3MOM\_noLF and 2MOM\_LF have similar frequency and 3MOM\_LF has the smallest. Smaller rain sizes are produced during melting in the stratiform precipitation region (at small precipitation rates  $< 2 \text{ mm hr}^{-1}$ ) with LF compared to noLF, a result that is consistent with Cholette et al. (2020) for a winter cyclone case simulated using P3. For precipitation rates between 2 and  $9 \text{ mm hr}^{-1}$ , there is higher frequency for LF for both 2MOM and 3MOM, with 3MOM\_LF having the highest frequency and 2MOM\_noLF the lowest. 3MOM\_LF has the highest spatial mean accumulation, followed by 2MOM\_LF, 3MOM\_noLF and 2MOM\_noLF, respectively, which agrees well with Figure 9. Differences among the 1-km simulations, shown in the caption of

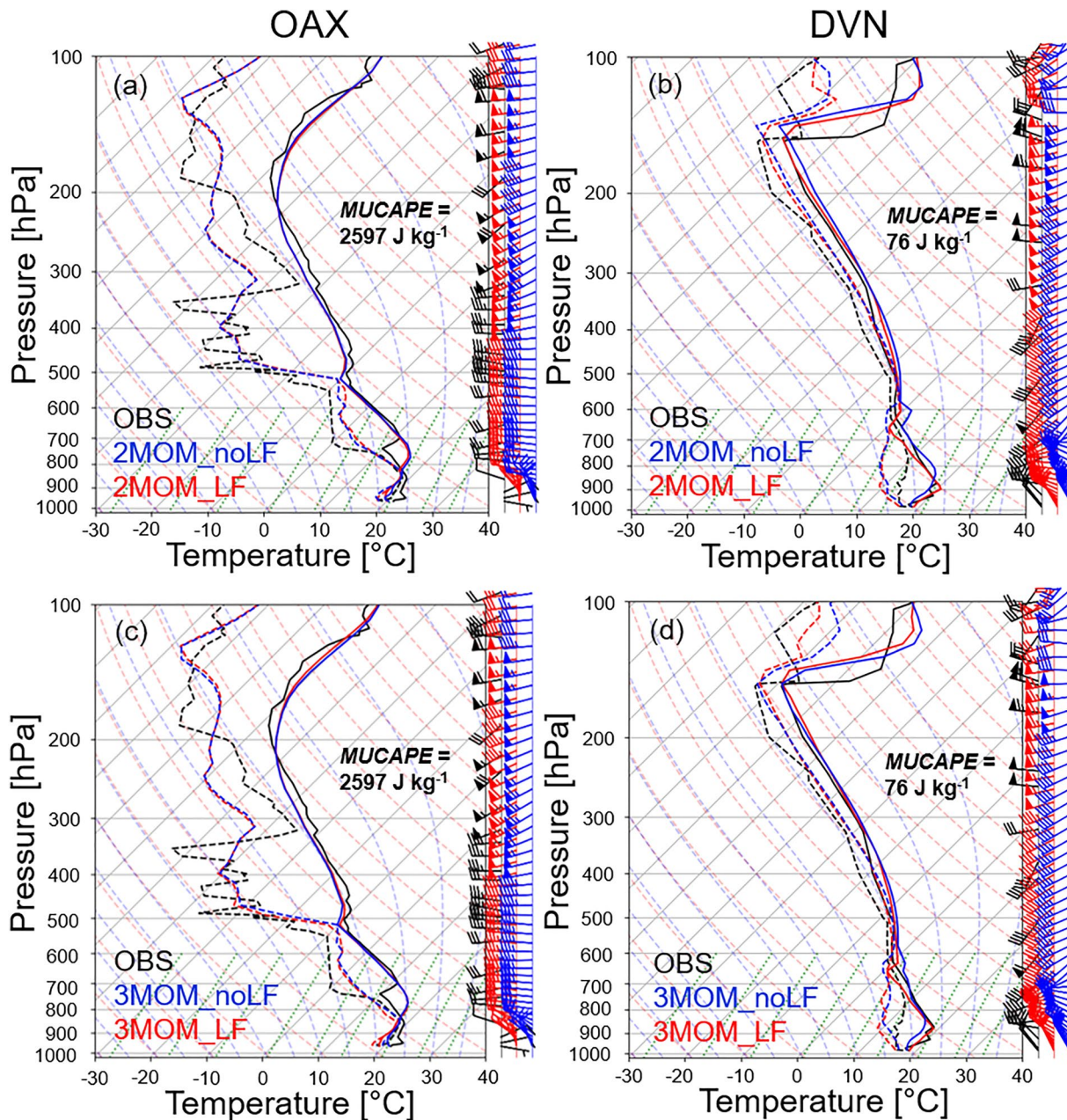


**Figure 7.** Soundings at OAX, (a and c), and DVN, (b and d), on 12 UTC 18 August 2019 from observations (black), noLF (blue) and LF (red) simulations. The 2MOM simulations are shown in (a and b), and the 3MOM simulations in (c and d). Solid lines are temperature [ $^{\circ}\text{C}$ ], dashed lines are dew point temperature [ $^{\circ}\text{C}$ ], and the wind barbs are in knots, with flags, pennants, and half-pennants denoting 50, 10, and 5 knots, respectively. The most unstable CAPE (MUCAPE) from the observed sounding is indicated in each panel. At OAX, MUCAPE values are 2,538, 2,505, 2,674, 2276  $\text{J kg}^{-1}$  for 2MOM\_noLF, 2MOM\_LF, 3MOM\_noLF and 3MOM\_LF, respectively. At DVN, MUCAPE values are 0, 6, 0, 7  $\text{J kg}^{-1}$  for 2MOM\_noLF, 2MOM\_LF, 3MOM\_noLF and 3MOM\_LF, respectively.

Figure 8, are between 0.1% and 4.3%, with the smallest difference between 2MOM\_LF and 3MOM\_noLF and the largest between 3MOM\_LF and 2MOM\_noLF.

Ice (hail) accumulation at the surface (Figure 10) is higher for 3MOM compared to 2MOM both with and without prediction of liquid fraction. The inclusion of mixed-phase particles with LF, however, reduces the amount of ice accumulated at the surface compared to noLF for both 2MOM and 3MOM. The decrease in ice accumulation with LF is due to smaller mean ice particle size near the surface in the convective region. This is a consequence of the melting process, during which the mass-weighted mean diameter of ice decreases with LF compared to noLF (C19, Cholette et al., 2020). In general, the melting level in the simulated storm is around 4-km AGL. Between

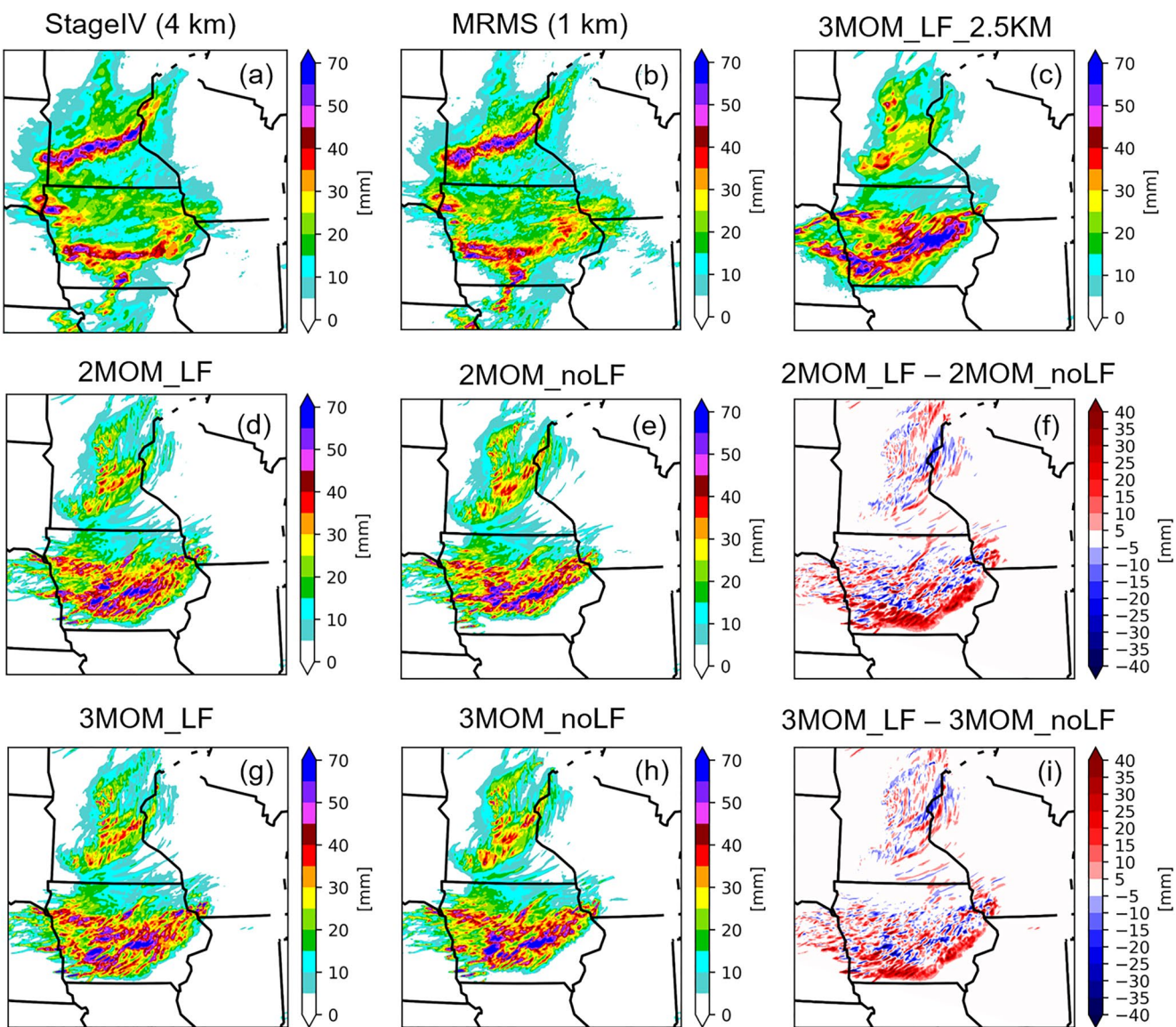


**Figure 8.** Precipitation accumulation from 04 to 10 UTC 18 August 2019 for (a) StageIV, (b) MRMS, (c) 3MOM\_LF\_2.5KM, (d) 2MOM\_LF, (e) 2MOM\_noLF, (g) 3MOM\_LF, and (h) 3MOM\_noLF. (f) Shows the difference 2MOM\_LF–2MOM\_noLF and (i) shows the difference 3MOM\_LF–3MOM\_noLF. The spatial means are 7.82, 8.77, 8.62, 8.86, 8.85, 8.99, and 9.39 mm for MRMS, StageIV, 2MOM\_noLF, 2MOM\_LF, 3MOM\_noLF, 3MOM\_LF, and 3MOM\_LF\_2p5, respectively.

3 and 4 km, where melting rates are the highest in all simulations, mean mass-weighted fall speed increases and mean mass-weighted diameter decreases with LF, whereas both are nearly constant with noLF. This can be seen in Figure S6 in Supporting Information S1, which shows the temporal mean vertical profiles spatially averaged over the convective cold pool area, as defined in Section 3.2 and analyzed in detail in the next Section 5.2. When the melting rate is reduced (below 3.5 km), the fall speed stops increasing as the diameter continues to decrease with LF. This results in smaller particle sizes and lower fall speed at the surface, which leads to a decrease in precipitation rate and ice accumulation compared to noLF simulations. These results will be examined in greater detail in a future study focusing on simulated hailstorms.

## 5.2. Reflectivity and Cold Pool

Compared to radar observations from the KARX and KDVN radars, all of the 1-km simulations overestimate reflectivity at 1 km height in the precipitating stratiform region (Figures 11 and 12). The 1-km simulations accentuate the bow aspect of the squall line compared to the 3MOM\_LF\_2.5KM (Figures 11b–11e and

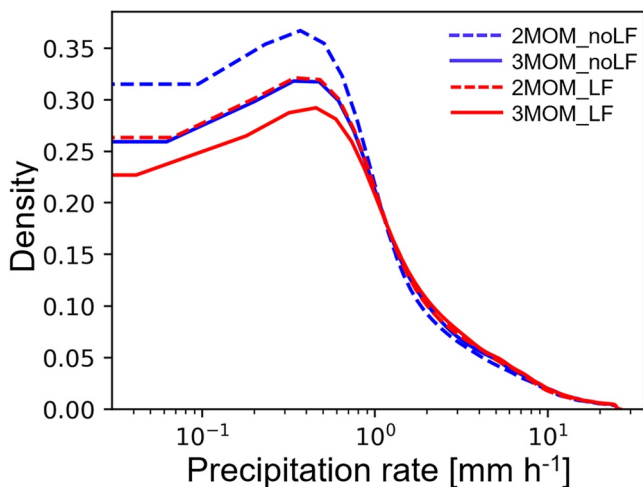


**Figure 9.** Kernel density estimate of hourly precipitation rates [ $\text{mm h}^{-1}$ ] for 3MOM\_LF (red), 2MOM\_LF (dashed red), 3MOM\_noLF (blue) and 2MOM\_noLF (dashed blue).

ones. The 3MOM\_LF bright band has lower reflectivity values than 2MOM\_LF due to the differences in ice above the  $0^\circ\text{C}$  level, which agrees better with observations, particularly in Figure 12. The ice reflectivity in the convective region (between  $x = 50$  and  $75$  km at  $10$  UTC; Figure 12) is higher with LF compared to noLF, which is supported by the contoured by frequency altitude diagrams (Figures S2f and S2h in Supporting Information S1) near  $3$ – $4$  km AGL. Observed reflectivity in the convective region peaks around  $65$  dBZ near  $x = 50$  km at  $6$  km height and near  $x = 100$  km at  $3$  km height in Figure 12. The  $6$  km height peak is well simulated by both 2MOM\_LF and 3MOM\_LF, underestimated by 3MOM\_noLF, and not captured by 2MOM\_noLF. Figures S3f, S3g, S3m, and S3n in Supporting Information S1 shows the same cross-sections but with the original calculation of equivalent reflectivity for simulations with LF. Differences in reflectivity structure are a combination of the direct effects of having modified the reflectivity calculation in regions of  $F_{i,\text{liq}} > 0$  and the indirect impacts of the different P3 configurations on the squall line structure and evolution with LF and 3MOM.

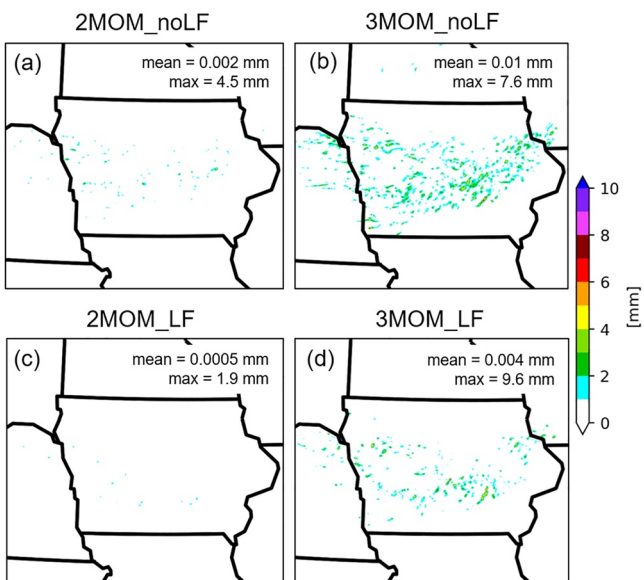


**Figure 10.** Ice accumulation from  $04$  to  $10$  UTC  $18$  August  $2019$  for (a) 2MOM\_noLF, (b) 3MOM\_noLF, (c) 2MOM\_LF and (d) 3MOM\_LF.

Figures 11b–11e), which compares better to the observed reflectivity structure. For both times shown in Figures 11 and 12, the freezing level is around  $4,000$  m, with slightly higher freezing level in the convective region. The reflectivity contribution from ice just above the freezing level in the stratiform precipitation region is smaller for 3MOM compared to 2MOM for both LF and noLF, which leads to smaller rain reflectivity below the melting level consistent with M21. In general, both ice and rain reflectivity are higher with 2MOM compared to 3MOM, and 3MOM simulations are closer to observations than 2MOM. The lower ice reflectivity aloft in the stratiform precipitation region is a consequence of smaller mean mass-weighted ice particle diameters in 3MOM compared to 2MOM for both noLF and LF (Figure S1 in Supporting Information S1). The systematic nature of this result as well as the link with the upper air transport of particles requires further investigation with other storms.

In Figure 11f, the observed reflectivity in the bright band is between  $40$  and  $50$  dBZ, with maxima near  $75$  and  $125$  km (in the  $x$ -direction). In Figure 12f, the observed bright band has lower reflectivity ( $35$ – $40$  dBZ) around  $x = 160$  km. The melting layer bright band is clearly visible for both 2MOM\_LF (Figures 11h, 11l, 12h, and 12l) and 3MOM\_LF (Figures 11j, 11n, 12j, and 12n) and the overall values of reflectivity compare well with the observed

Time series of the cold pool parameters computed as described in Section 3.2 are shown in Figure 13. The idealized cold pool speed  $C$  (Figure 13a) is higher by about  $0.5$ – $2$   $\text{m s}^{-1}$  in 3MOM\_LF compared to the other simulations.  $C$  is similar between 3MOM\_LF and 2MOM\_LF while it increases with LF compared to noLF for both 2MOM and 3MOM. Differences between the simulations in  $C$  are similar to those obtained for the actual moving speed of the squall line. The simulated squall lines move about  $60$ – $66$   $\text{km hr}^{-1}$ , with 2MOM\_noLF being the slowest ( $60$   $\text{km hr}^{-1}$ ) and 3MOM\_LF the fastest ( $66$   $\text{km hr}^{-1}$ ). The propagation speed is  $\sim 0.5$   $\text{m s}^{-1}$  greater in 3MOM\_noLF than in 2MOM\_noLF. With LF, the propagation speed is  $1$ – $1.5$   $\text{m s}^{-1}$  faster compared to noLF for both 2MOM and 3MOM. The mean perturbation potential temperature is lower by about  $0.2$ – $0.9^\circ\text{C}$  with LF compared to noLF (Figure 13c) in the analyzed cold pool region. The depth of the cold pool is generally lower with LF than noLF (Figure 13b).

The differences in cold pool speed between the simulations are mainly due to the thermal term in (11) since similar results as Figure 13 are obtained when only the thermal buoyancy is considered for computing  $C$  (not shown). Therefore, we analyze the contributions of the microphysical processes responsible for cooling in the cold pool region of each simulation (i.e., ice sublimation, melting, mixed-phase particles evaporation, rain evaporation and cloud evaporation); results are shown in Figure 14 for the total cooling

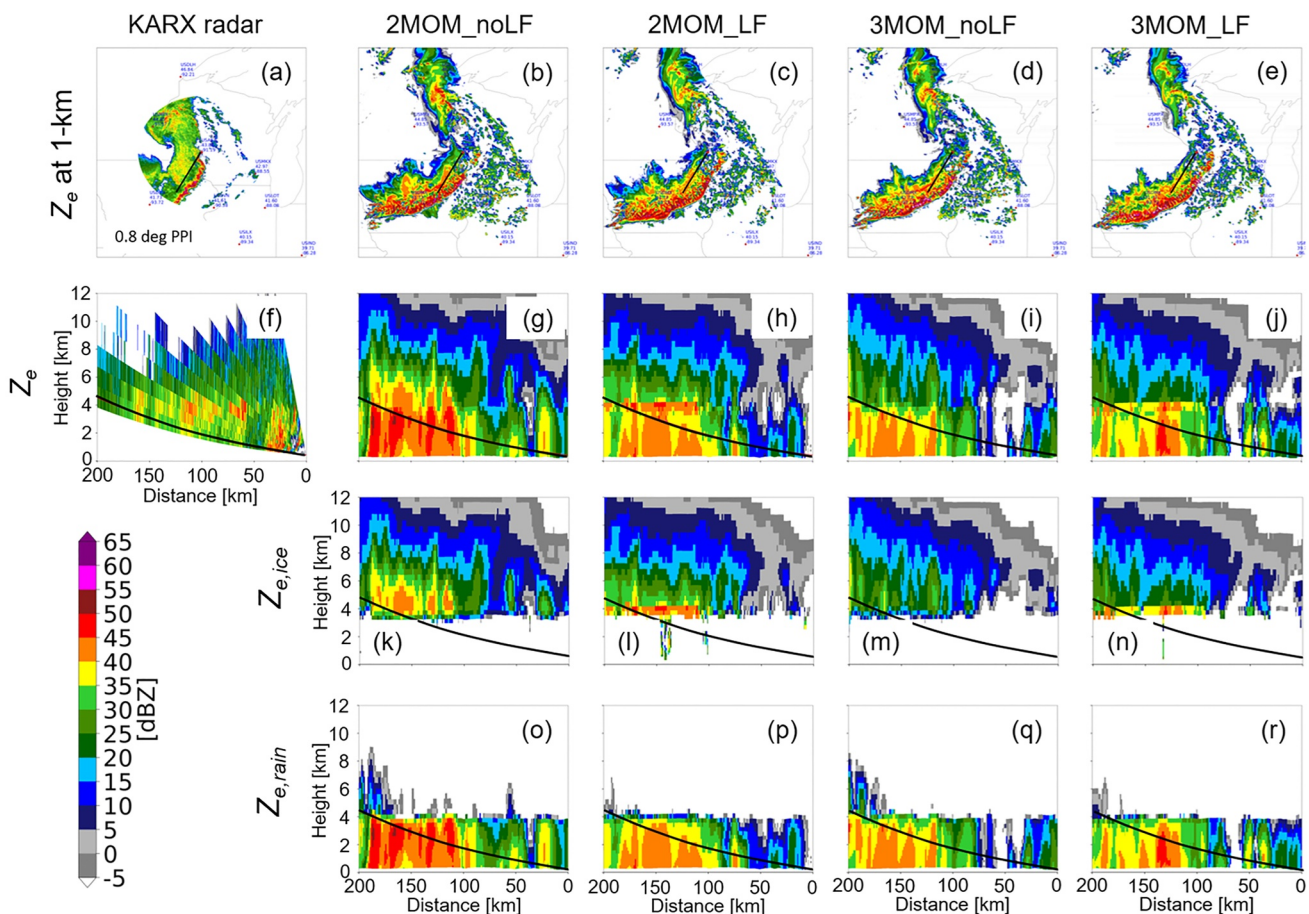


**Figure 11.** (a) Observed reflectivity from KARX radar at 1-km height ( $Z$ , [dBZ]) and (b–e) simulated equivalent reflectivity at  $\sim$ 1-km height ( $Z_e$ , [dBZ]) at 09 UTC 18 August 2019 for the 1-km simulations: (b) 2MOM\_noLF, (c) 2MOM\_LF, (d) 3MOM\_noLF and (e) 3MOM\_LF. (f–r) Vertical cross-section of (f) KARX radar, (g–j) total equivalent reflectivity ( $Z_e$ , [dBZ]), (k–n) ice or mixed-phase particle equivalent reflectivity ( $Z_{e,ice}$ , but expressed in dBZ) and (o–r) rain equivalent reflectivity ( $Z_{e,rain}$ , but expressed in dBZ) for (g, k, and o) 2MOM\_noLF, (h, l, and p) 2MOM\_LF, (i, m, and q) 3MOM\_noLF, and (j, n, and r) 3MOM\_LF at 09 UTC 18 August 2019. Locations of the vertical cross sections in (f–r) are shown by the southwest-to-northeast oriented black lines in (a–e).

and in Figure 15 for each process contribution (Figure 15 shows results from the 3MOM simulations only since similar results are obtained for 2MOM).

For noLF simulations (Figures 14a and 14b), the cooling peak near 4 km height is from ice sublimation and the second peak near 3 km is due to melting. In contrast, for LF simulations (Figures 14c and 14d) there is only one peak near 3.5 km, suggesting that the transition between sublimation and melting is smoother (Figures 15b and 15h). Below 3 km, for all simulations the dominant cooling process is rain evaporation (Figures 15c and 15d). Peak cooling rates in the melting region are clearly greater for LF than noLF, particularly at 08 UTC (Figure 14). Cooling from melting is slightly greater for noLF compared to LF (Figures 15g and 15h). With LF, it is the combination of ice sublimation, melting, and mixed-phase particle evaporation that is the main driver of greater cooling rates in this region (Figures 15b, 15h, and 15i). Mixed-phase particle evaporation is considered in LF but neglected in noLF (since it does not represent mixed-phase particles), and contributes 5%–15% of the total latent cooling within the melting region in both 2MOM\_LF and 3MOM\_LF (Figure 15i). Ice sublimation is not allowed at  $T > 0^\circ\text{C}$  with noLF, while it is allowed with LF. Melting can be delayed in both LF and noLF when humidity is low, and ice sublimation can occur in LF simulations in this situation when  $F_{i,\text{liq}} < 0.01$ . At any temperature, condensation/evaporation of mixed-phase particles can occur when  $F_{i,\text{liq}} \geq 0.01$  in LF. Therefore, the region of ice sublimation is larger and extends to more levels below  $0^\circ\text{C}$ , further increasing the total latent cooling. Also, at  $T > 0^\circ\text{C}$ , rain evaporation (Figures 15c and 15d) begins at lower vertical levels in LF compared to noLF for both 2MOM and 3MOM because mixed-phase particles are formed instead.

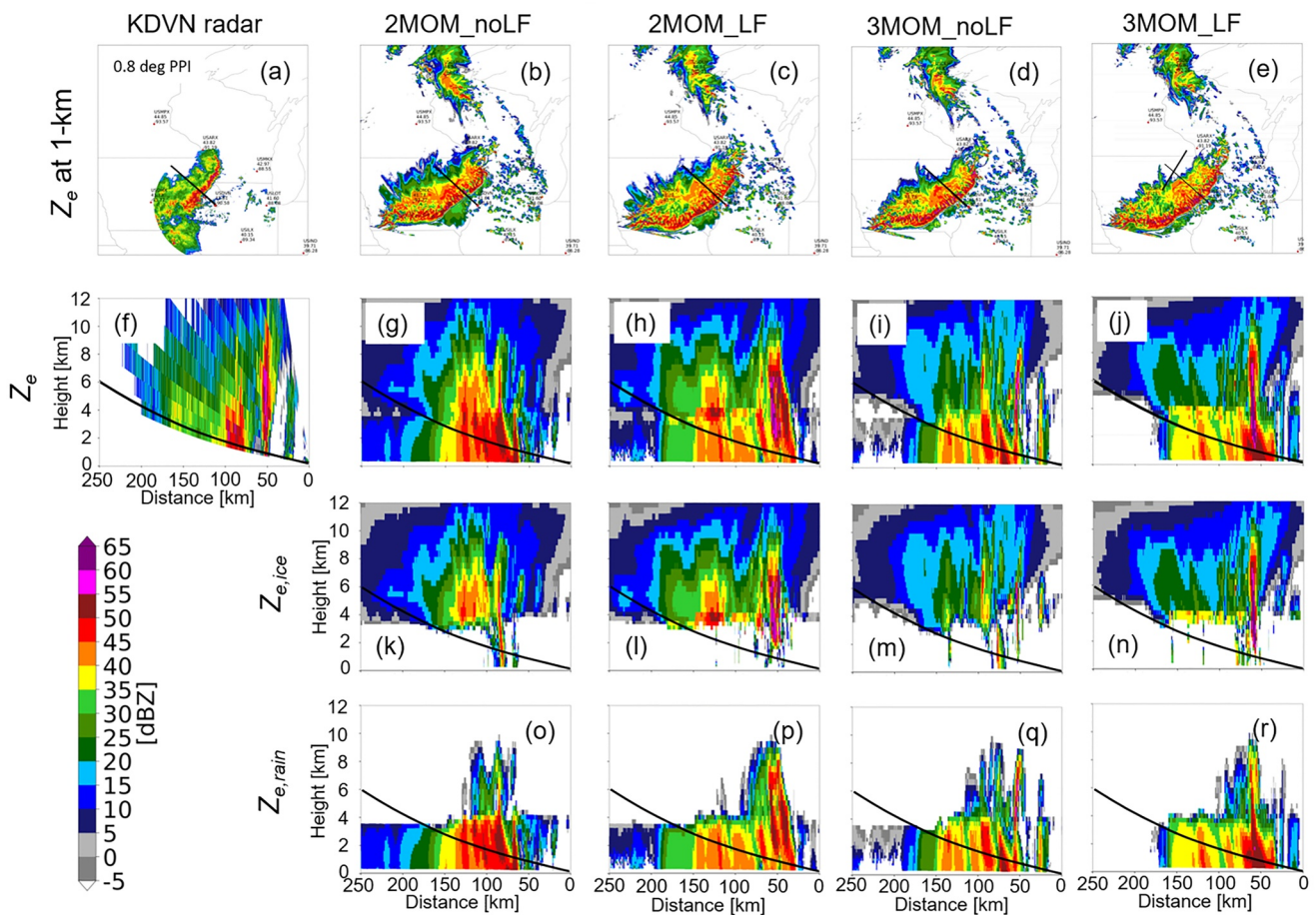


**Figure 12.** As in Figure 11 but at 10 UTC 18 August 2019 and compared with KDVN radar.

To evaluate the impacts of mixed-phase particle evaporation and ice sublimation processes on the cold pool speed and cooling rates, two sensitivity simulations were conducted. The first is with 3MOM\_noLF but allowing ice sublimation/deposition at  $T > 0^\circ\text{C}$  (called 3MOM\_noLF\_SUBT>0). The second uses 3MOM\_LF but neglects evaporation/condensation of mixed-phase particles (called 3MOM\_LF\_NOQLEVP). Figure S4 in Supporting Information S1 shows results in the same format as Figure 13, but only for the 3MOM simulations and sensitivity tests. Mean vertical profiles of cooling and warming terms are also shown in Figure S5 in Supporting Information S1 for the four 3MOM simulations. Adding sublimation at  $T > 0^\circ\text{C}$  with noLF produces results closer to 3MOM\_LF by increasing the cold pool speed and reducing the potential temperature. This indicates that ice sublimation/deposition at  $T > 0^\circ\text{C}$  is an important process for the cold pool parameters. However, the cold pool speed remains slower compared to 3MOM\_LF because allowing sublimation/deposition at  $T > 0^\circ\text{C}$  impacts other processes as well (Figures S5a and S5b in Supporting Information S1). Mainly, there is less rain evaporation with 3MOM\_noLF\_SUBT>0 compared to 3MOM\_noLF both in regions where there is sublimation (generally  $>3$  km) and below. This reduces cooling and leads to a similar cold pool speed despite the additional cooling from sublimation. Removing evaporation/condensation of mixed-phase particles alone has almost no impact on the cold pool speed and potential temperature. It sometimes increases the speed (such as at 08 UTC) while at other times reduces it (such as at 06 UTC). When the cold pool speed is increased in 3MOM\_LF\_NOQLEVP, there is a small increase in cooling from rain evaporation (Figure S5c in Supporting Information S1) below 3 km. When the depth of the cold pool is higher and more similar between the simulations (e.g., at 06 UTC for LF simulations; Figure S4 in Supporting Information S1), warming processes aloft (between 4 and 5 km) play a more important role in cold pool evolution. The warming processes are condensation (rain, cloud, mixed-phase particles), refreezing of mixed-phase particles, and ice deposition. Then, the cold pool speed can be smaller in 3MOM\_LF\_NOQLEVP compared to 3MOM\_LF because no condensation of mixed-phase particles occurs and

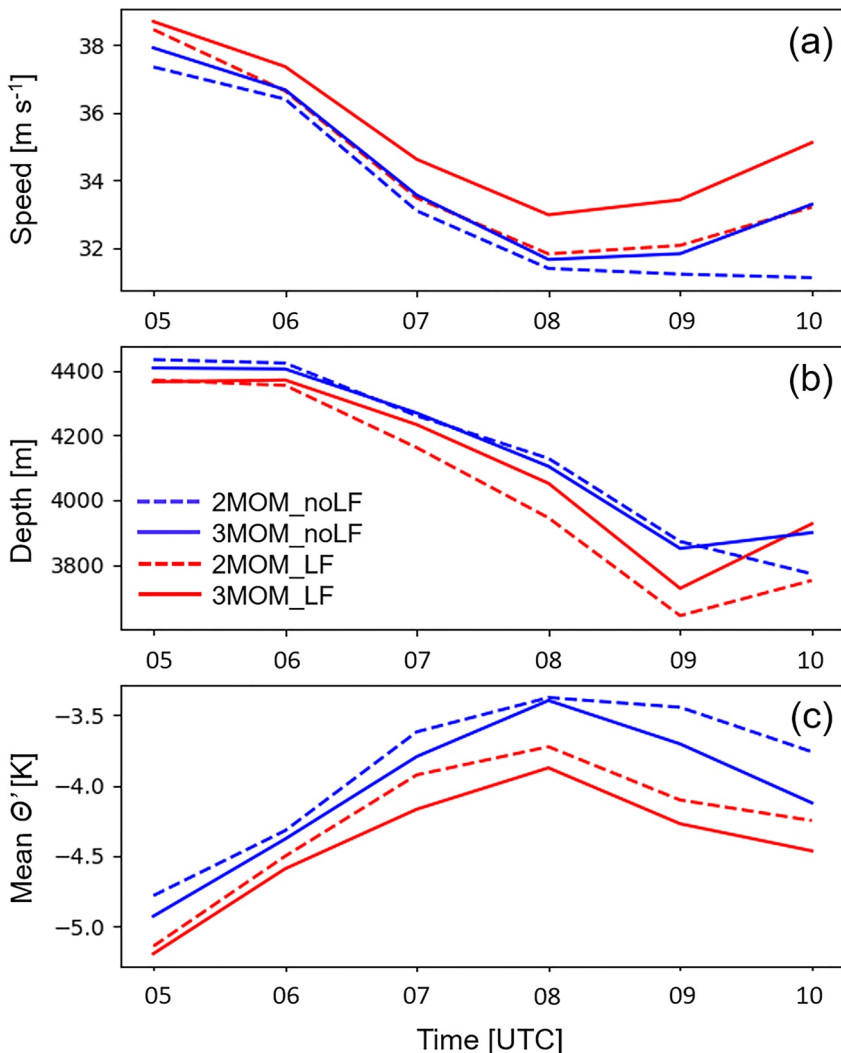


**Figure 13.** Time series of (a) idealized cold pool speed  $C$  [ $\text{m s}^{-1}$ ], (b) cold pool depth [m] and (c) mean potential temperature perturbation ( $\theta'$ ; [K]) for 2MOM\_noLF (dashed blue), 3MOM\_noLF (blue), 2mom\_LF (dashed red) and 3MOM\_LF (red). The cold pool parameters are calculated over cold pool regions as described in Section 3.2.

there is less refreezing. We conclude that the stronger cold pool with LF compared to noLF is due to the combination of many microphysical processes and their interactions.

## 6. Conclusions

The P3 microphysics scheme has been further developed and now combines the triple-moment treatment of ice with predicted liquid fraction of ice (now mixed-phase) particles. Predicting a third independent moment of the ice particle size distribution allows the distribution shape parameter to vary freely, while predicting the liquid fraction allows for an explicit representation of mixed-phase hydrometeors. This update includes modifications to some triple-moment process rates, which are now different when the liquid fraction is non-zero. P3 has also been updated to include a generalized computation of the equivalent reflectivity, which accounts for the liquid component of mixed-phase particles. This new version of P3 has been tested and the impacts of the combined modifications examined in the context of 1-km mesoscale model simulations of a mid-latitude squall line.

Both the triple-moment and liquid fraction ice-phase components have notable impacts on the dynamics and microphysics of the simulated convective system. There is an increase of accumulation of frozen precipitation at the surface with the triple-moment option, both with and without the predicted liquid fraction. In contrast, there

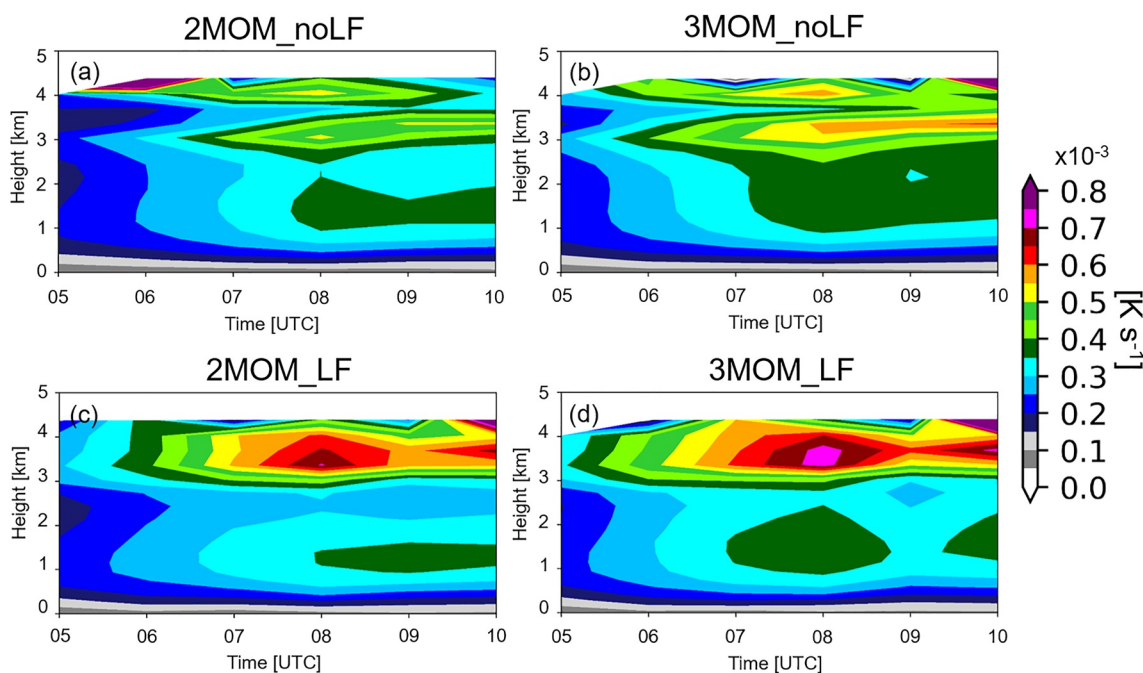


**Figure 14.** Time series of vertical profiles of total latent cooling rates from the microphysics spatially averaged over the cold pool region calculated in Figure 13 (i.e., sum of ice sublimation, mixed-phase particle evaporation, melting, cloud evaporation and rain evaporation, [ $\text{K s}^{-1}$ ]) for (a) 2MOM\_noLF, (b) 3MOM\_noLF, (c) 2MOM\_LF, and (d) 3MOM\_LF.

is a decrease in ice-phase precipitation with the predicted liquid fraction. This result is from a decrease of the mean mass-weighted diameter of ice during melting with the predicted liquid fraction that reduces the precipitation rate and accumulation of ice/mixed-phase particles in the convective precipitation region. Cold pools are stronger (i.e., lower cold pool temperature) and propagation speeds are higher when liquid fraction is predicted and mixed-phase particles are simulated. This is a consequence of more intense cooling from the microphysics at levels just below the  $0^\circ\text{C}$  isotherm. The higher cooling rates are associated with a larger extent of ice sublimation and the additional process of mixed-phase particle evaporation. This leads to a faster propagation of the squall lines by  $\sim 0.5\text{--}2 \text{ m s}^{-1}$  when liquid fraction is predicted and mixed-phase particles are represented.

The presence of liquid in mixed-phase particles significantly affects the simulated reflectivity structure due to the change in the scattering properties (backscattering cross-section), which improves the simulation of the bright band - the region of enhanced reflectivity in the melting region. Changes in reflectivity structure are not only a direct result of the change in scattering properties by representing mixed-phase particles, but also from the change in squall line structure and evolution. The reflectivity parameterization described here does not account for attenuation (e.g., Luo et al., 2022). Although this study only examined a single case, the changes to reflectivity structure and the bright band with predicted liquid fraction are consistent with expected behavior, and likely to be general. A more in-depth analysis of the simulated bright band (e.g., Shrestha et al., 2022) could include changing the options for the parameterization of particle properties (e.g., mixture and inclusion) in the equivalent reflectivity calculations of P3. While there is evidence from this case study that the reflectivity structure is generally improved, no claims can be made that the overall model performance is improved or deteriorated. Rather, an understanding of the sensitivity to new changes in the microphysics scheme can be seen.

Both the triple-moment approach and the inclusion of a predicted liquid fraction have been shown to improve the overall realism in representing microphysical processes in P3 (C19; M21), and the results of this study clearly indicate that these components affect the simulation of linear mesoscale convective systems. The effects of these new options on hail merit further study, particularly since the impacts of the liquid fraction component on hail have not been examined yet in detail. Hail forecasting using numerical models continues to be a challenge and is an important high-impact weather element in many parts of the world (Allen et al., 2020). Given the parameterization improvements in treating melting and wet growth by predicting liquid fraction in mixed-phase particles, it is expected that these new aspects will be important in cloud-resolving simulations of hailstorms. The

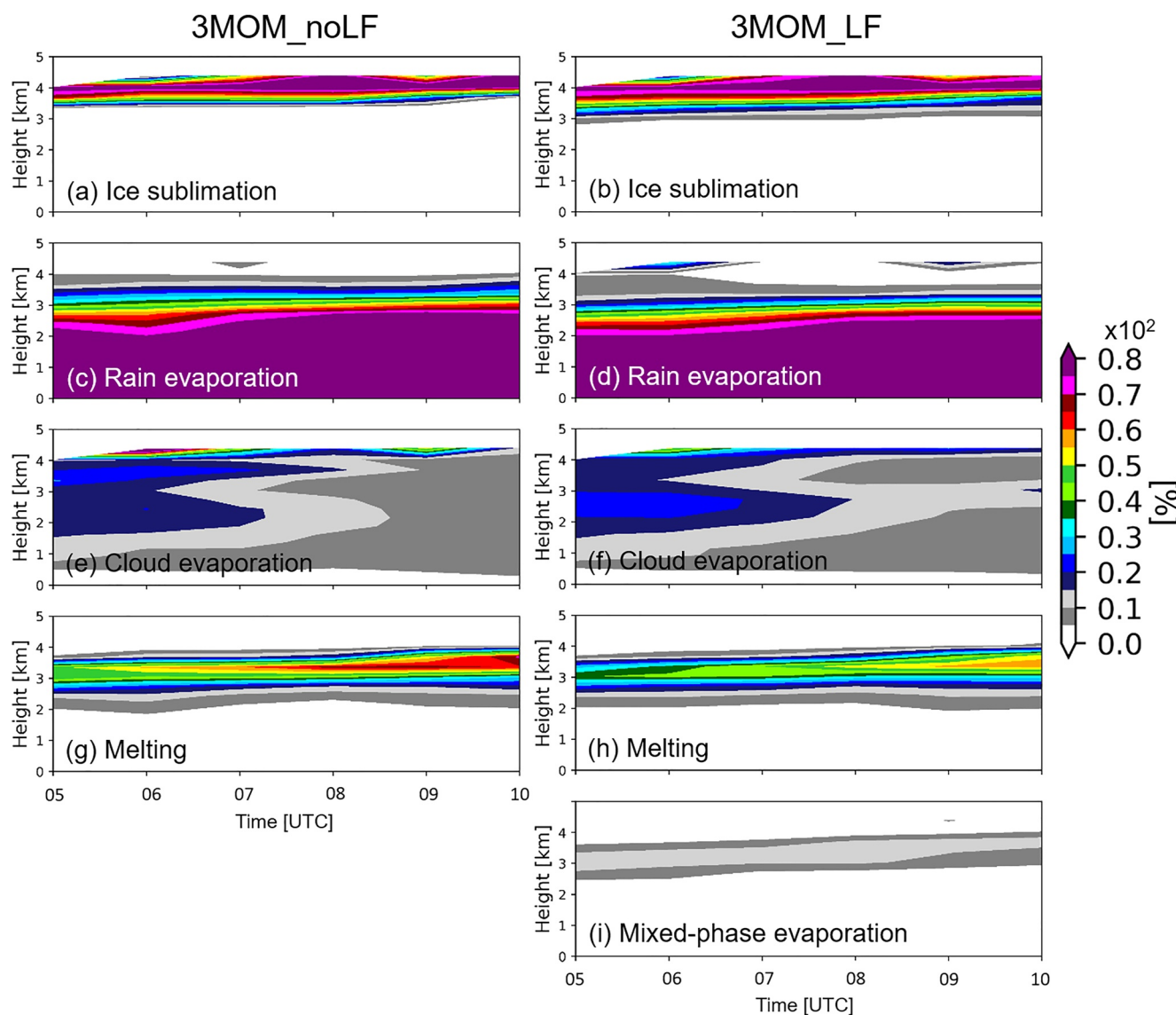


**Figure 15.** Time series of vertical profiles of latent cooling rates from the microphysics (expressed in % relative to the total latent cooling rate) spatially averaged over the cold pool region: (a, b) ice sublimation, (c, d) rain evaporation, (e, f) cloud evaporation, (g, h) melting and (i) mixed-phase particle evaporation. Results from 3MOM\_noLF are shown in the left column (a, c, e, g) and from 3MOM\_LF in (b, d, f, h, i). Note that mixed-phase particle evaporation is only included in 3MOM\_LF.

impacts of the updated P3 in the simulation of hail, along with the contributing effects of including multiple free ice-phase/mixed-phase categories, is the subject of on-going investigation using real and idealized cases and will be presented in future publications.

We conclude with a comment on the computational cost of using these new options in P3, since computation speed is an ever-present concern in models, and for NWP in particular. It was shown in Morrison et al. (2015) with direct timing comparisons between WRF simulations with different microphysics schemes that the original P3 was faster than other state-of-the-art BMSs. This was due to the combination of the extensive use of lookup tables in P3 in place of the direct (and costly) calculations of process rates (e.g., integrals over the size distribution) during run-time and the relatively low number of prognostic (i.e., advected) variables. In this study, we have added two optional prognostic variables to the ice (mixed-phase) category, for up to six variables per category. Although the single category is used here, we allude to the use of this configuration with multiple categories in P3. This will no doubt raise concern about the added computational cost, particularly for models with Eulerian advection schemes, such as WRF. However, with the specific choice of these prognostic variables, P3 lends itself increasingly well to benefit from the “scaled flux vector transport” method described in Morrison et al. (2016),

where most of the cost of advection comes from the regular advection of a single lead variable. In this case, the lead variable is the total ice mass mixing ratio ( $q_{i,\text{tot}}$ ), with only a relatively small additional cost for the advection of the other prognostic variables for that ice category. Thus, despite the increasing detail and complexity through on-going developments including those described here, P3 continues to be computationally competitive and with room for considerable optimization in some models in terms of coupling with advection.

## Appendix A

(See Table A1).

**Table A1**  
*Descriptions of Variables and Their Units*

Symbol	Description	Units
$\alpha_{\text{va}}$	Coefficient for unrimed non-spherical ice particle mass	$\text{kg m}^{-\beta_{\text{va}}}$
$B$	Buoyancy	$\text{m}^2 \text{s}^{-2}$
$\beta_{\text{air}}$	Air coefficient for $\epsilon_{\text{eff}}$	—
$\beta_{\text{ice}}$	Ice coefficient for $\epsilon_{\text{mix1}}$	—
$B_{i,\text{rim}}$	Rime volume mixing ratio of ice	$\text{m}^3 \text{kg}^{-1}$
$\beta_{\text{va}}$	Coefficient for unrimed non-spherical ice particle mass	—
$C$	Cool pool speed	$\text{m s}^{-1}$
CAPE	Convective available potential energy	$\text{J kg}^{-1}$
$D$	Equivalent-volume diameter of ice particles	m
$D_{\text{cr}}$	Threshold diameter fully rimed spherical ice particles from partially rimed non-spherical ice particles in the ice size distribution	m
$D_a$	Diameter of the ice core of mixed-phase particles	m
$D_{\text{eq}}$	Spherical equivalent diameter	m
$D_{\text{gr}}$	Threshold diameter separating unrimed non-spherical ice particles from fully rimed spherical ice particles in the ice size distribution	m
$D_m$	Mean mass-weighted diameter of the ice category	cm
$D_{\text{th}}$	Threshold diameter separating small spherical ice particles from unrimed non-spherical ice particles in the ice size distribution	m
$D_{\text{thrs}}$	Threshold diameter for the shape parameter Equation B2	m
$\epsilon_{\text{air}}$	Dielectric constant of air for $\epsilon_{\text{eff}}$	—
$\epsilon_{\text{eff}}$	Effective relative dielectric constant of the mixture	—
$\epsilon_i$	Dielectric constant of solid ice	—
$\epsilon_{\text{ice}}$	Dielectric constant of ice for $\epsilon_{\text{mix1}}$	—
$\epsilon_{\text{mix1}}$	Dielectric constant of mixture #1 (water and ice)	—
$\epsilon_w$	Dielectric constant of water	—
$\epsilon_{\text{water}}$	Dielectric constant of water for $\epsilon_{\text{mix1}}$	—
$F_{i,\text{liq}}$	Bulk liquid mass fraction	—
$F_{i,\text{rim}}$	Bulk rime mass fraction	—
$g$	Gravitational acceleration	$\text{m s}^{-2}$
$\overline{H}$	Mean depth of the cold pool	m
$K_i$	Dielectric factor of ice	—
$K_w$	Dielectric factor of water	—
$\lambda$	Slope parameter in P3 ice size distribution	$\text{m}^{-1}$
$\lambda_0$	Radar wavelength	m
$m(D)$	Mass-D relationship of ice particles	kg
$m_a(D)$	Mass-D relationship of the ice core component of mixed-phase particles	kg
$m_{\text{eff}}$	Effective refractive index	—

**Table A1**  
*Continued*

Symbol	Description	Units
$m_{\text{liq}}(D)$	Mass-D relationship for liquid drops ( $F_{i,\text{liq}} = 1$ )	kg
$m_i(D, F_{i,\text{liq}})$	Mass-D relationship of whole mixed-phase particles	kg
MUCAPE	Most unstable convective available potential energy	J kg <sup>-1</sup>
$N_0$	Intercept parameter the ice size distribution	kg <sup>-1</sup> m <sup>-1</sup>
$N_c$	Cloud number mixing ratios	# kg <sup>-1</sup>
$N(D)$	Ice particle size distribution	# kg <sup>-1</sup> m <sup>-1</sup>
$N_{i,\text{tot}}$	Total ice number mixing ratio	kg <sup>-1</sup>
$N_r$	Rain number mixing ratios	# kg <sup>-1</sup>
$\rho_g$	Density of fully rimed ice	kg m <sup>-3</sup>
$\rho_i$	Density of ice (spherical)	kg m <sup>-3</sup>
$\rho_{\text{ice}}$	Density of ice as given by the $m(D)$ relationship	kg m <sup>-3</sup>
$\rho_{i,\text{rim}}$	Rime density	kg m <sup>-3</sup>
$\rho_m$	Mean density	kg m <sup>-3</sup>
$\rho_{\text{sph.ice}}$	Density of small spherical ice	kg m <sup>-3</sup>
$\rho_w$	Liquid water density	kg m <sup>-3</sup>
$q_c$	Cloud mass mixing ratio	kg kg <sup>-1</sup>
$q_{i,\text{dep}}$	Ice mass mixing ratio growing by vapor diffusion	kg kg <sup>-1</sup>
$q_{i,\text{ice}}$	Ice mass mixing ratio	kg kg <sup>-1</sup>
$q_{i,\text{liq}}$	Liquid mass mixing ratio accumulated on ice	kg kg <sup>-1</sup>
$q_{i,\text{rim}}$	Rime mass mixing ratio	kg kg <sup>-1</sup>
$q_{i,\text{tot}}$	Total mass mixing ratio of ice and mixed-phase particles	kg kg <sup>-1</sup>
$q_r$	Rain mass mixing ratio	kg kg <sup>-1</sup>
$q_x$	Mass mixing ratio of ice, snow or graupel if $x = i, s$ or $g$ , respectively	kg kg <sup>-1</sup>
$q_{x,k\_above\_0}$	Mass mixing ratio at the level just above the 0°C level of ice, snow or graupel if $x = i, s$ or $g$ , respectively	kg kg <sup>-1</sup>
$q_v$	Water vapor mixing ratio	kg kg <sup>-1</sup>
$\overline{q}_v$	Spatially average water vapor mixing ratio	kg kg <sup>-1</sup>
$\sigma_b(D)$	Backscattering cross-section as a function of $D$	m
$\sigma_b(D_{\text{eq}})$	Backscattering cross-section as a function of $D_{\text{eq}}$	m
$T$	Air temperature	°C
$\theta$	Potential temperature	K
$\bar{\theta}$	Spatially-averaged potential temperature	K
$\theta'$	Perturbed potential temperature ( $\theta - \bar{\theta}$ )	K
$\mu$	Shape parameter the ice size distribution	—
$\mu_c$	Shape parameter the cloud size distribution	—
$\mu_r$	Shape parameter the rain size distribution	—
$V$	Total volume assuming spherical	m <sup>3</sup>
$V_{\text{air}}$	Partial volume of air (total mixture)	—
$V_{\text{ice}}$	Partial volume of ice (mixture #1)	—
$V_{\text{ice,comp}}$	Volume of ice component in the whole mixture	m <sup>3</sup>
$V_m$	Mean mass-weighted fall speed of the ice category	m s <sup>-1</sup>
$Vol_{\text{air}}$	Partial volume of air (total mixture)	—
$Vol_{\text{ice}}$	Partial volume of ice (total mixture)	—
$Vol_{\text{water}}$	Partial volume of water (total mixture)	—

**Table A1**  
*Continued*

Symbol	Description	Units
$V_{w,\text{comp}}$	Volume of water component in the whole mixture	$\text{m}^3$
$Z$	Radar reflectivity (observed)	$\text{dBZ}$
$Z_e$	Equivalent reflectivity	$\text{dBZ}$
$Z_{e,\text{ice}}$	Ice reflectivity factor	$\text{m}^6 \text{ kg}^{-1}$
$Z_{e,\text{rain}}$	Rain reflectivity factor	$\text{m}^6 \text{ kg}^{-1}$
$Z_{i,\text{tot}}$	6th-moment mixing ratio	$\text{m}^6 \text{ kg}^{-1}$

## Appendix B: Baseline Configuration of P3

The P3 scheme uses a particle property-based approach for each ice category. The bulk ice particles evolve freely and smoothly from small spherical ice to fully rimed ice particles through the processes of vapor diffusion and rime growth. P3 started with the 2-moment single ice category version, described in detail in MM15, followed by the generalized multiple ice-category configuration, described in Milbrandt and Morrison (2016). Over the following few years, there were some major further developments to P3, summarized in Figure B1. These include: the prediction of the bulk liquid mass fraction to allow for mixed-phase particles (C19); the triple-moment treatments of rain, which improves the simulation of convective rain cores (Paukert et al., 2019); the subgrid-scale diagnostic of the cloud and precipitation fractions, for use at coarser horizontal resolutions (Jouan et al., 2020); and the triple-moment treatment of ice, which improves the simulation of hail (M21).

The liquid fraction and triple-moment rain options were built from the main P3 development stream. To date, triple-moment rain has not yet been integrated into the “official” version of P3. The liquid fraction option has now been integrated on top of version 4 (v4; Figure B1) to produce v5. In this study, the baseline version of P3 refers to v5 but with the following configuration selections: 1 ice category, the cloud and precipitation fraction diagnostic off, 2-moment ice, and liquid fraction off. Note, this is equivalent to v4 with the same options.

### B1. Details of Baseline Version

P3 is 2-moment for cloud droplets ( $N_c, q_c$ ) and raindrops ( $N_r, q_r$ ), with  $N$  and  $q$  representing the number and the mass mixing ratios, respectively. Liquid phase processes, such as droplet nucleation, condensation/evaporation, autoconversion, accretion, self-collection, breakup of raindrops, and homogenous and heterogeneous freezing of cloud droplets and rain, follow the parameterization described in MM15. Homogenous and heterogeneous freezing of cloud droplets and rain can occur at temperatures below  $-40^\circ\text{C}$  and  $-4^\circ\text{C}$ , respectively.

The baseline configuration is also 2-moment for the ice category ( $N_{i,\text{tot}}, q_{i,\text{tot}}$ ). Two other prognostic bulk variables are used to quantify the rimed portion of the ice category: the mass and rime volume mixing ratios (i.e.,  $q_{i,\text{rim}}$ ;  $B_{i,\text{rim}}$ ) in the baseline version.

The conservation equation for any prognostic microphysical variable  $X$  is

$$\frac{\partial X}{\partial t} = -u \cdot \nabla X + \frac{1}{\rho_a} \frac{\partial(\rho_a V_X X)}{\partial z} + \Delta^*(X) + \left. \frac{dX}{dt} \right|_S \quad (\text{B1})$$

where  $t$  is time,  $\rho_a$  is the air density,  $u$  is the 3D wind vector,  $z$  is height,  $V_X$  is the mass-weighted fall speed,  $\Delta^*(X)$  is a subgrid-scale mixing operator and  $\left. \frac{dX}{dt} \right|_S$  is a source/sink term that includes various microphysical processes.

In the original version of the P3 scheme, the shape parameter  $\mu$  of the ice size distribution (Equation 2) was a function of the slope parameter (Equation B2) following Heymsfield (2003), and bounded between 0 and 6:

$$\mu = 0.00191 \lambda^{0.8} - 2 \quad (\text{B2})$$

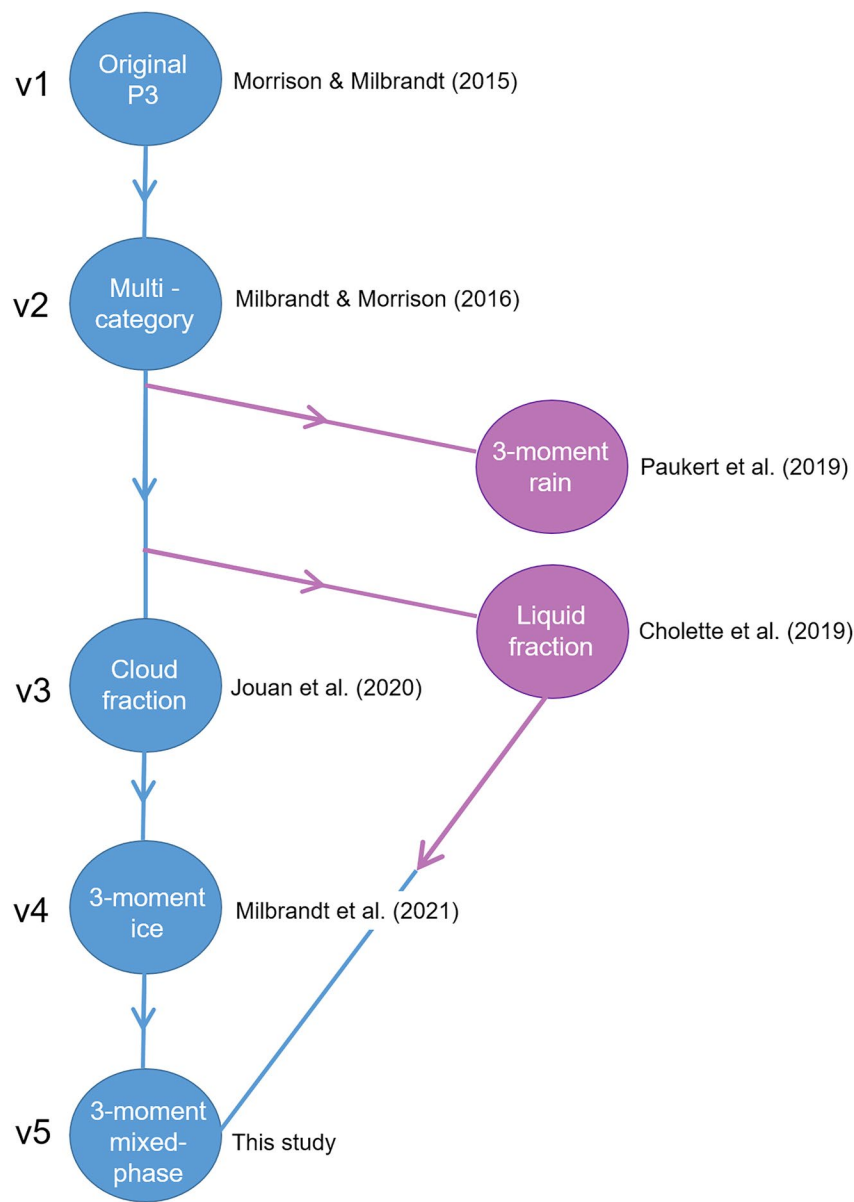


**Figure B1.** Flow chart of the major stages of the development of P3. Blue denotes the main development stream of development; pink denotes independent research developments.

Since M21 and based on the comparison with the 3-moment treatment of ice, a new diagnostic relationship for the shape parameter is used:

$$\mu = \begin{cases} \text{Eq. (B2), for } D_{\text{eq}} \leq D_{\text{thrs}} \\ \max[1, 1 + 0.00842(\rho_m - 400)] 0.25(D_{\text{eq}} - D_{\text{thrs}}) F_{i,\text{rim}}, \text{ for } D_{\text{eq}} > D_{\text{thrs}} \end{cases} \quad (\text{B3})$$

with  $D_{\text{thrs}} = 0.0002$  m,  $\rho_m$  is the mean ice density (assumed to be equals to  $\rho_g$ ; see MM15 for details) and  $D_{\text{eq}} = \left( \frac{6q_{i,\text{tot}}}{\pi\rho_m N_{i,\text{tot}}} \right)^{1/3}$  is the mean-mass diameter assuming spherical volume. An upper limit of 20 is imposed to  $\mu$  for  $D_{\text{eq}} > D_{\text{thrs}}$ . Note that Equation B3 differs slightly from the original equation in M21 which contains a typographical error.

The mass-diameter relationship ( $m(D)$ ) used to obtain  $q_{i,\text{tot}}$  is divided in up to four parts depending on the bulk state (unrimed, partially-rimed or fully rimed):

$$m(D) = \begin{cases} \frac{\pi}{6} \rho_i D^3; & \text{if } D \leq D_{\text{th}} : \text{small spherical ice} \\ \alpha_{\text{va}} D^{\beta_{\text{va}}}; & \text{if } D_{\text{th}} < D \leq D_{\text{gr}} : \text{unrimed nonspherical ice} \\ \frac{\pi}{6} \rho_g D^3; & \text{if } D_{\text{gr}} < D \leq D_{\text{cr}} : \text{fully rimed spherical ice} \\ \frac{\alpha_{\text{va}} (1 + F_{i,\text{rim}})}{1 - F_{i,\text{rim}}} D^{\beta_{\text{va}}}; & \text{if } D > D_{\text{cr}} : \text{partially rime nonspherical ice} \end{cases} \quad (\text{B4})$$

where  $\rho_i = 917 \text{ kg m}^{-3}$ ,  $\alpha_{\text{va}} = 0.0121$  and  $\beta_{\text{va}} = 1.9$  (Brown & Francis, 1995; Hogan et al., 2012). The three critical diameters ( $D_{\text{th}}$ ,  $D_{\text{gr}}$  and  $D_{\text{cr}}$ ) are given in MM15 or by Equations 4 of C19. A similar approach to  $m(D)$  and a division into the four parts of the size distribution is used for the terminal velocity-, the projected area-, the capacitance- and the ventilation coefficients-diameter relationships.

Ice-phase processes common to all P3 options include vapor transfer at  $T < 0^\circ\text{C}$  (deposition/sublimation), melting, nucleation processes, dry and wet collection with rain and cloud, for which there is some shedding in wet growth situations, and sedimentation.

## B2. Triple-Moment Ice

The optional 3-moment ice in v4 and v5, described in M21, aims at improving the simulations of hail-type particle properties in convective situations. It also helps controlling the size-sorting effect in BMS by solving for an additional moment of the size distribution, which determines the shape parameter. In P3, this new prognostic moment is the sixth moment,  $Z_{i,\text{tot}}$  ( $\text{m}^6 \text{ kg}^{-1}$ ). The diagnostic shape parameter used in the 2-moment configuration (Equation B3) is no longer needed as  $\mu$  is now computed from three ice prognostic variables as:

$$G(\mu) = \frac{(6 + \mu)(5 + \mu)(4 + \mu)}{(3 + \mu)(2 + \mu)(1 + \mu)} = \frac{N_{i,\text{tot}} Z_{i,\text{tot}}}{\left( \frac{\sigma q_{i,\text{tot}}}{\pi \rho_m} \right)^2} \quad (\text{B5})$$

for which  $\mu$  is bounded between 0 and 20. The value of  $\mu$  is obtained using a piecewise polynomial approximation of Equation B5, based on seven precomputed second-degree polynomials (curve fits to numerically-determined solutions) within the bounded range. This method, originally developed by Milbrandt and Yau (2005), gives  $\mu$  with relative errors generally less than 1% (and absolute errors less than 0.1). More mathematically elegant approaches have also been used to solve for  $\mu$  in triple-moment schemes (e.g., Loftus et al., 2014; Paukert et al., 2019; Shan et al., 2020). However, our polynomial approximation method is simple, sufficiently accurate, and computationally efficient.

Microphysical processes are divided into three groups for the  $Z_{i,\text{tot}}$  closure assumptions (M21). In the first group, that is, the ice initiation processes, a fixed value of the shape parameter is specified for the new portion of ice initiated, from which the tendency of  $Z_{i,\text{tot}}$  is obtained. For ice nucleation, the assigned value of  $\mu$  is 10. For homogeneous and heterogeneous freezing of cloud or rain,  $\mu$  is equal to current the value of  $\mu_c$  or  $\mu_r$ , respectively. For the second group, that is, the growth and decay processes (sublimation, deposition, melting, collection with rain and cloud, and ice self-collection), the  $Z_{i,\text{tot}}$  tendency is obtained by assuming that the net change in  $\mu$  is negligible compared to the impact from processes in the other groups, so the shape parameter remains constant during the time step ( $d\mu/dt|_{\text{group 2}} = 0$ ). The third group is the tendency for  $Z_{i,\text{tot}}$  due to sedimentation, which is calculated explicitly based on the  $Z_{i,\text{tot}}$ -weighted mean fallspeed.  $Z_{i,\text{tot}}$  tendencies for the three groups are given in M21 with Equations 9–11.

## B3. Prediction of the Bulk Liquid Fraction

The original development of a new prognostic mixing ratio for the liquid mass on ice ( $q_{i,\text{liq}}$ ) to represent mixed-phase particles evolution while predicting the bulk liquid mass fraction ( $F_{i,\text{liq}}$ ) is described in C19 (built off of v2 of P3; see Figure B1). The three assumptions with the predicted  $F_{i,\text{liq}}$  that also apply to the 3-moment treatment described in Section 2 are summarized as follows. First, as for  $F_{i,\text{rim}}$ , the liquid fraction of each particle

of the size distribution does not vary with size and is equal to the bulk liquid fraction  $F_{i,\text{liq}}$ . Second, the liquid water is uniformly distributed around an ice core and the ice core has the same properties (mass, projected area, capacitance, ventilation coefficient and so on) as if no liquid fraction is predicted. Therefore, the third assumption is that some processes, such as melting and sublimation/deposition, depend on the ice core properties while the other processes, such as refreezing and vapor condensation of  $q_{i,\text{liq}}$ , depend on properties of the whole mixed-phase particle.

Both the ice core and the whole particle size distributions are given by Equation 2 using Equation B2 for the shape parameter, but with different  $\rho_m$  and  $D_{\text{vd}}$ . For instance,  $\rho_m = \rho_g$  and  $D_{\text{vd}} = \left(\frac{6(1-F_{i,\text{liq}})q_{i,\text{tot}}}{\pi\rho_g N_{i,\text{tot}}}\right)^{1/3}$  for the ice core distribution and  $\rho_m = (1 - F_{i,\text{liq}})\rho_g + F_{i,\text{liq}}\rho_w$  (assuming a linear function with  $F_{i,\text{liq}}$  and  $\rho_w = 1,000 \text{ kg m}^{-3}$ ) and  $D_{\text{vd}} = \left(\frac{6q_{i,\text{tot}}}{\pi\rho_m N_{i,\text{tot}}}\right)^{1/3}$  for the whole mixed-phase particle size distribution. Equation B4 with  $D = D_d$  (the ice portion diameter) is used for the ice core particle size distribution. For processes acting on whole mixed-phase particles, the mass-diameter relationship (C19) is

$$m_t(D, F_{i,\text{liq}}) = (1 - F_{i,\text{liq}}) m_d(D) + F_{i,\text{liq}} m_{\text{liq}}(D) \quad (\text{B6})$$

with  $m_d(D)$  given by Equation B4. Here  $D$  is the diameter of the entire mixed-phase particle, and  $m_{\text{liq}}(D) = \pi/6\rho_w D^3$  with  $\rho_w = 1,000 \text{ kg m}^{-3}$ .

The differences in the microphysical process parameterizations with the predicted  $F_{i,\text{liq}}$ , compared to the standard version without liquid fraction, are as follows. First, the melting source/sink terms are divided into two terms. The first term (QRMLT) is the melted water transferred into rain from the complete melting of small spherical ice particles (Rasmussen et al., 1984a), and the second term (QIMLT) is the melted water that accumulates on ice following Fujiyoshi (1986). When  $F_{i,\text{liq}} > 0.99$ , all the remaining ice mass and number are transferred to rain. Without the predicted liquid fraction, all the melted water mass produced in a time step is instantaneously transferred to  $q_r$ . The ice number mixing ratio sink and rain number mixing ratio source terms associated with the melted water transferred to rain are proportional to the respective changes in  $q_{i,\text{ice}}$  for all versions.

The second difference is the refreezing process (QLFRZ), which provides the rate of accumulated water that refreezes when  $T < 0^\circ\text{C}$ : this process is neglected when mixed-phase particles are not parameterized. The refreezing is computed following Pruppacher and Klett (1997) using relationships for the capacitance and the ventilation coefficient that includes both the ice and the liquid components of mixed-phase particles. The mass of mixed-phase particles that refreeze from  $q_{i,\text{liq}}$  in one time step is transferred to the rimed portion of the ice  $q_{i,\text{rim}}$ .

Third, at  $T > 0^\circ\text{C}$ , the masses of cloud droplets (QLCOLLC) and rain (QLCOLLR) that collide with ice are accumulated in  $q_{i,\text{liq}}$ , whereas mass is shed assuming shed drop of 1 mm size (Rasmussen et al., 1984b) without predicting liquid fraction. At  $T < 0^\circ\text{C}$ , in wet growth situations and without predicted liquid fraction, not all of the collected liquid water is frozen into  $q_{i,\text{rim}}$  and some fraction is shed instead (Musil, 1970). With prediction of liquid fraction, collected rain and cloud (QLWGRTH) is a source of  $q_{i,\text{liq}}$  and shedding of accumulated liquid water from both melting and wet growth occurs when  $F_{i,\text{rim}} > 0$  (i.e., for rimed particles). It is assumed that only ice particles with diameters  $> 9 \text{ mm}$  within the particle size distribution shed liquid water (Rasmussen et al., 1984b) (QLSHD).

Fourth, with predicted liquid fraction, deposition/sublimation of ice is allowed only when  $F_{i,\text{liq}} = 0$  because liquid water is assumed to be distributed evenly around the ice core when  $F_{i,\text{liq}} > 0$ ; condensation/evaporation (QLCON and QLEVP, respectively) of the liquid mass mixing ratio  $q_{i,\text{liq}}$  occurs when  $F_{i,\text{liq}} > 0$ , the latter being neglected without predicting liquid fraction. Sublimation/deposition and condensation/evaporation can occur at any temperature with predicted liquid fraction, whereas sublimation/deposition of ice occurs only at  $T < 0^\circ\text{C}$  without liquid fraction prediction. Finally, other ice phase processes such as self-aggregation and crystal nucleation (at  $T < -15^\circ\text{C}$ ) are parameterized the same with and without predicted liquid fraction following MM15.

All other ice-phase processes, such as self-aggregation and nucleation, and liquid-phase (cloud and rain) processes, such as droplet nucleation, vapor transfers, autoconversion, accretion, self-collection, break-up, homogenous freezing and heterogeneous freezing, are parameterized as described in MM15 (details given in C19).

The microphysical tendency equation for  $q_{i,\text{liq}}$  is

$$\frac{dq_{i,\text{liq}}}{dt} \Big|_S = \text{QIMLT} + \text{QLWGRTH} + \text{QLCON} + \text{QLCOLLR} + \text{QLCOLLC} - \text{QLFRZ} - \text{QUEVP} - \text{QLSHD} \quad (\text{B7})$$

where QIMLT is melting, QLWGRTH is wet growth, QLCON is condensation, QLCOLLR (QLCOLLC) is collection of rain (cloud droplets), QLSHD is shedding, QLFRZ is refreezing and QUEVP is evaporation. Note that, during a given time step, the portion of melted water that is transferred to rain (QRMLT) is not yet included in the rain condensation/evaporation process as the mass has not been transferred yet to the rain category. This mass may undergo mixed-phase particle condensation/evaporation.

### Appendix C: Equivalent Reflectivity

The simulated total equivalent reflectivity [dBZ] in P3 without the predicted liquid fraction is given by

$$Z_e = 10 \log [(Z_{e,\text{rain}} + Z_{e,\text{ice}}) * 10^{18}] \quad (\text{C1})$$

where  $Z_{e,\text{rain}}$  is the equivalent reflectivity factor of the rain distribution and  $Z_{e,\text{ice}}$  is the equivalent reflectivity factor of the ice distribution. The general formula for  $Z_{e,\text{ice}}$  is (e.g., Huang et al., 2021)

$$Z_{e,\text{ice}} = \frac{|K_i|^2}{|K_w|^2} \int_0^\infty \left( \frac{\rho_{\text{ice}}}{\rho_i} \right)^2 D_{\text{eq}}^6 N(D_{\text{eq}}) dD_{\text{eq}} \quad (\text{C2})$$

where  $\rho_{\text{ice}}$  is the density of the ice crystal determined using the mass-diameter relationship,  $\rho_i = 917 \text{ kg m}^{-3}$  is the density of solid ice sphere and  $D_{\text{eq}}$  is the equivalent spherical diameter.  $N(D_{\text{eq}})$  is the ice crystal size distribution expressed as a function of  $D_{\text{eq}}$ . The mass-diameter relationship is  $m(D) = m(D_{\text{eq}}) = \frac{\pi}{6} \rho_{\text{ice}} (D_{\text{eq}}) D_{\text{eq}}^3$  and by replacing  $\rho_{\text{ice}}^2 D_{\text{eq}}^6$  in Equation C2 with  $\left(\frac{6}{\pi} m(D)\right)^2$ , the following equation is obtained:

$$Z_{e,\text{ice}} = \frac{|K_i|^2}{|K_w|^2} \int_0^\infty \left( \frac{6}{\pi \rho_i} \right)^2 m(D)^2 N(D_{\text{eq}}) dD_{\text{eq}} \quad (\text{C3})$$

with  $D$  being the diameter of ice particles. If one considers the ice size distribution as a function of  $D$ , the following equivalent form to Equation C3 is used:

$$Z_{e,\text{ice}} = \frac{|K_i|^2}{|K_w|^2} \int_0^\infty \left( \frac{6}{\pi \rho_i} \right)^2 m(D)^2 N(D) dD \quad (\text{C4})$$

where  $K_w = \frac{\epsilon_w - 1}{\epsilon_w + 2}$  is the dielectric factor of water, which is a function of the dielectric constant of water ( $\epsilon_w$ ). The typical value of  $|K_w|^2$  is 0.93 at 0°C and for a radar wavelength between 5 and 10 cm.  $K_i = \frac{\epsilon_i - 1}{\epsilon_i + 2}$  is the dielectric factor of solid ice and it is, as for water, assumed to be constant ( $|K_i|^2 = 0.176$ ). The mass-diameter relationship in P3 is a function of the four parts of the particle size distribution (see MM15 for details) and given by Equation B4, while  $N(D)$  is given by Equation 2.

For particles composed of a mixture of material, an effective (or averaged) scattering is needed to express the equivalent reflectivity factor  $Z_{e,\text{ice}}$ . Numerous formulations of the dielectric factor for mixtures have been obtained empirically and depend on the choice of the particle mixture. For particles composed of a mixture of air, water and ice, the equivalent radar reflectivity factor (Blahak, 2016) is given by

$$Z_{e,\text{ice}} = \frac{\lambda_0^4}{\pi^5 |K_w|^2} \int_0^\infty \sigma_b(D_{\text{eq}}) N(D_{\text{eq}}) dD_{\text{eq}}. \quad (\text{C5})$$

Following the logic of Equation C4, we write Equation C5 as

$$Z_{e,\text{ice}} = \frac{\lambda_0^4}{\pi^5 |K_w|^2} \int_0^\infty \sigma_{b,D}(D) N(D) dD \quad (\text{C6})$$

where  $\lambda_0$  is the radar wavelength (10 cm) and  $\sigma_b(D_{\text{eq}})$  (or  $\sigma_{b,D}(D)$ ) is the backscattering cross-section of a particle having a spherical equivalent diameter  $D_{\text{eq}}$  (or a diameter  $D$ ). The typical value of  $|K_w|^2$  is 0.93 at 0°C and for a radar wavelength between 5 and 10 cm. For  $D_{\text{eq}} < \lambda_0$ , the Rayleigh-approximation is used and  $\sigma_b$  is

$$\sigma_b(D_{\text{eq}}) = \frac{\pi^5}{\lambda_0^4} \left| \frac{m_{\text{eff}}^2 - 1}{m_{\text{eff}}^2 + 2} \right|^2 D_{\text{eq}}^6 = \frac{\pi^5}{\lambda_0^4} |K_i|^2 D_{\text{eq}}^6 \quad (\text{C7})$$

with  $|K_i| = \left| \frac{m_{\text{eff}}^2 - 1}{m_{\text{eff}}^2 + 2} \right| = \left| \frac{\epsilon_{\text{eff}} - 1}{\epsilon_{\text{eff}} + 2} \right|$ . The backscattering cross-section is a function of the particle shape (and diameter), the radar wavelength and the particle effective refractive index ( $m_{\text{eff}}^2 = \epsilon_{\text{eff}}$ , with  $\epsilon_{\text{eff}}$  being the effective relative dielectric constant).

As in WRF, the Maxwell-Garnett formula (Bohren & Huffman, 1983; Garnett, 1904) is used to compute  $\epsilon_{\text{eff}}$ . The method consists of calculating two dielectric constants to find the average effective refractive index. The mixture and its inclusion form are the user's choice in the code used to generate the P3 lookup table. In this study, spheroidal inclusions are assumed.

We first calculate a dielectric factor  $\epsilon_{\text{mix1}}$  that assumes a mixture of ice and water, with water being the matrix and ice the inclusion:

$$\epsilon_{\text{mix1}} = \frac{(1 - V_{\text{ice}})\epsilon_{\text{water}} + V_{\text{ice}}\epsilon_{\text{ice}}\beta_{\text{ice}}}{1 - V_{\text{ice}} + V_{\text{ice}}\beta_{\text{ice}}} \quad (\text{C8})$$

where  $\beta_{\text{ice}} = \left( \frac{2\epsilon_{\text{water}}}{\epsilon_{\text{ice}} - \epsilon_{\text{water}}} \right) \left[ \frac{\epsilon_{\text{ice}}}{\epsilon_{\text{ice}} - \epsilon_{\text{water}}} \log \left( \frac{\epsilon_{\text{ice}}}{\epsilon_{\text{water}}} \right) - 1 \right]$  and  $V_{\text{ice}} = \frac{\text{Vol}_{\text{ice}}}{\text{Vol}_{\text{water}} + \text{Vol}_{\text{ice}}}$  is the partial volume of ice component in the water/ice mixture particle. This is then used to calculate an effective refractive index  $m_{\text{eff}}$  from  $\epsilon_{\text{eff}}$  that assumes a mixture of ice/water and air. The matrix is the mixture of ice and water (i.e.,  $\epsilon_{\text{mix1}}$ ) and the inclusion is air:

$$\epsilon_{\text{eff}} = \frac{(1 - V_{\text{air}})\epsilon_{\text{mix1}} + V_{\text{air}}\epsilon_{\text{air}}\beta_{\text{air}}}{1 - V_{\text{air}} + V_{\text{air}}\beta_{\text{air}}} \quad (\text{C9})$$

where  $\beta_{\text{air}} = \left( \frac{2\epsilon_{\text{mix1}}}{\epsilon_{\text{air}} - \epsilon_{\text{mix1}}} \right) \left[ \frac{\epsilon_{\text{air}}}{\epsilon_{\text{air}} - \epsilon_{\text{mix1}}} \log \left( \frac{\epsilon_{\text{air}}}{\epsilon_{\text{mix1}}} \right) - 1 \right]$  and  $V_{\text{air}} = \text{Vol}_{\text{air}}$ , the partial volume of the air component in the air plus water/ice particle mixture. The partial volumes of each component of the mixture are determined as follows:

$$\text{Vol}_{\text{ice}} = \frac{V_{\text{ice,comp}}}{V} \quad (\text{C10})$$

$$\text{Vol}_{\text{water}} = \frac{V_{\text{w,comp}}}{V} \quad (\text{C11})$$

$$\text{Vol}_{\text{air}} = 1 - \text{Vol}_{\text{ice}} - \text{Vol}_{\text{water}} \quad (\text{C12})$$

with  $V_{\text{ice,comp}} = \frac{m_{\text{ice,comp}}}{\rho_{\text{ice,comp}}} = \frac{m_t - m_w}{900}$ ,  $V_{\text{w,comp}} = \frac{m_{\text{w,comp}}}{\rho_{\text{w,comp}}} = \frac{m_w}{1000} = \frac{F_{i,\text{liq}} m_t}{1000}$ , where  $m_t = m_t(D, F_{i,\text{liq}})$  and is given by Equation B6.  $V = \frac{\pi}{6} D_{\text{eq}}^3$  is the total spherical equivalent volume of each particle in the distribution and  $D_{\text{eq}} = \left( \frac{6V}{\pi} \right)^{1/3}$ .

Figure C1 shows partial volumes (Equation C10–C12) as a function of the mixed-phase particle diameter for different combination of the  $F_{i,\text{liq}}$  and  $F_{i,\text{rim}}$ . The partial volumes depend on the  $m$ - $D$  relationship of various parts of the size distribution in P3 (see Equation B4). For example, for a given  $F_{i,\text{rim}}$  and  $F_{i,\text{liq}}$ , the partial volumes of air, water and ice are, respectively, 0,  $F_{i,\text{liq}}$  and  $(1 - F_{i,\text{liq}})$  where the particle density is  $900 \text{ kg m}^{-3}$  in the particle size distribution: this is the case for small pristine spherical ice particles (i.e., at  $D < D_{\text{th}}$ ). As  $D$  increases, and for ice regimes with non-constant density as a function of  $D$ , the partial volumes of ice and water decrease while the partial volume of air increases corresponding to decreasing particle density. For a given  $F_{i,\text{rim}}$ , the partial volume of air is smaller with greater  $F_{i,\text{liq}}$ , meaning that more air pockets are filled with meltwater as  $F_{i,\text{liq}}$  increases. The partial volume of air increases for a given  $D$  as  $F_{i,\text{rim}}$  decreases leading to a reduced particle density. The partial volume of the water component increases with  $F_{i,\text{liq}}$ . The main difference between the WRF and new P3 approaches is that the WRF approach has smaller  $\text{Vol}_{\text{air}}$ , but larger  $\text{Vol}_{\text{water}}$  and  $\text{Vol}_{\text{ice}}$ . For  $F_{i,\text{liq}} = 0.667$ ,  $\text{Vol}_{\text{air}}$  is 0 for both rime mass fractions of 0 and 1 (Figures C1b and C1d).

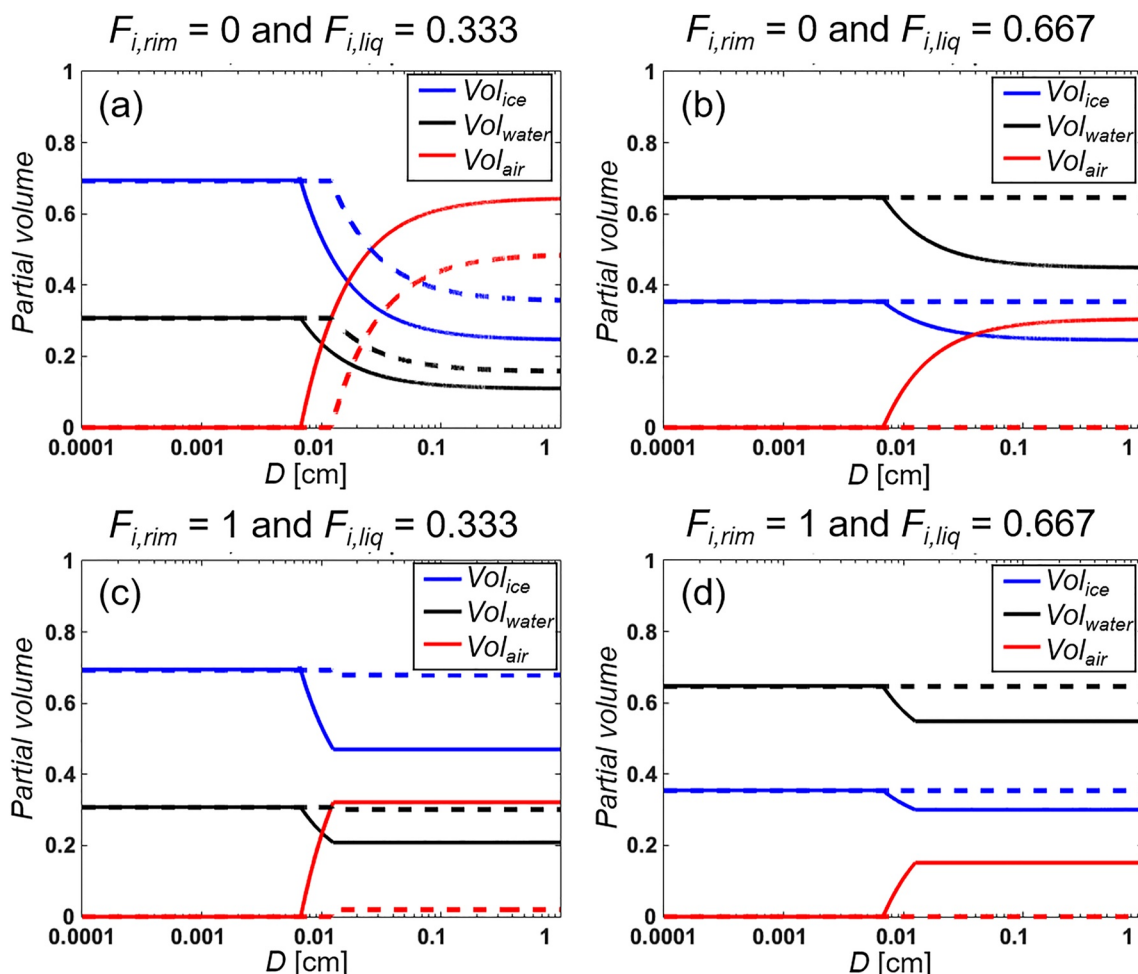


**Figure C1.** P3 (solid lines) and WRF (dashed lines) partial volume of the ice ( $\text{Vol}_{\text{ice}}$ ; blue), water ( $\text{Vol}_{\text{water}}$ ; black) and air ( $\text{Vol}_{\text{air}}$ ; red) components as a function of the particle diameter ( $D$ ; [cm]) for different combinations of rime ( $F_{i,\text{rim}}$ ) and liquid ( $F_{i,\text{liq}}$ ) mass fractions: (a, b)  $F_{i,\text{rim}} = 0$ , (c, d)  $F_{i,\text{rim}} = 1$ , and (a, c)  $F_{i,\text{liq}} = 0.333$  and (b, d)  $F_{i,\text{liq}} = 0.667$ . For (c, d), the rime density is  $450 \text{ kg m}^{-3}$ . The x-axis is logarithmic and the sum of the three partial volumes equals 1.

## Data Availability Statement

The 2-moment ice version of the P3 bulk microphysics scheme and the 3-moment ice version are available on the GEM publicly available GitHub repository (<https://github.com/ECCC-ASTD-MRD/gem>) and in the WRF model (available at [https://www2.mmm.ucar.edu/wrf/users/download/get\\_sources.html#WRF-ARW](https://www2.mmm.ucar.edu/wrf/users/download/get_sources.html#WRF-ARW)) (Skamarock et al., 2019), respectively. This version has been modified to include the predicted liquid fraction following Cholette et al. (2019). All data including those used to initialize the simulations, the simulated outputs, the Python plotting scripts, the BALTRAD product (Michelson et al., 2018), the ERA5 data (available at <https://confluence.ecmwf.int/display/CKB/How+to+download+ERA5>) (Hersbach et al., 2020), StageIV (available at <https://data.eol.ucar.edu/dataset/21.093>) (Du, 2011) and MRMS (available at <https://www.nssl.noaa.gov/projects/mrms/>) (Zhang et al., 2011) used in this study are archived internally for 5-year at the Canadian Meteorological Center. Soundings are available on the University of Wyoming web site (at <http://weather.uwyo.edu>).

## Acknowledgments

We appreciate the constructive comments from the two anonymous reviewers, and from Ted Mansell (the third reviewer), which led to improvements to the paper.

## References

- Adams-Selin, R. D., van den Heever, S. C., & Johnson, R. H. (2013a). Impact of graupel parameterization schemes on idealized bow echo simulations. *Monthly Weather Review*, 141(4), 1241–1262. <https://doi.org/10.1175/MWR-D-12-00064.1>
- Adams-Selin, R. D., van den Heever, S. C., & Johnson, R. H. (2013b). Sensitivity of bow-echo simulation to microphysical parameterizations. *Weather and Forecasting*, 28(5), 1188–1209. <https://doi.org/10.1175/WAF-D-12-00108.1>

- Allen, J. T., Giannanco, I. M., Kumjian, M. R., Jurgen Punge, H., Zhang, Q., Groenemeijer, P., et al. (2020). Understanding hail in the Earth system. *Reviews of Geophysics*, 58(1), e2019RG000665. <https://doi.org/10.1029/2019RG000665>
- Bao, J. W., Michelson, S. A., & Grell, E. D. (2019). Microphysical process comparison of three microphysics parameterization schemes in the WRF model for an idealized squall-line case study. *Monthly Weather Review*, 147(9), 3093–3120. <https://doi.org/10.1175/MWR-D-18-0249.1>
- Bélair, S., Crevier, L. P., Mailhot, J., Bilodeau, B., & Delage, Y. (2003). Operational implementation of the ISBA land surface scheme in the Canadian regional weather forecast model. Part I: Warm season results. *Journal of Hydrometeorology*, 4(2), 352–370. [https://doi.org/10.1175/1525-7541\(2003\)4<352:OIOTIL>2.0.CO;2](https://doi.org/10.1175/1525-7541(2003)4<352:OIOTIL>2.0.CO;2)
- Bélair, S., Mailhot, J., Girard, C., & Vaillancourt, P. (2005). Boundary layer and shallow cumulus clouds in a medium-range forecast of a large-scale weather system. *Monthly Weather Review*, 133(7), 1938–1960. <https://doi.org/10.1175/MWR2958.1>
- Benjamin, S. G., Weygandt, S. S., Brown, J. M., Hu, M., Alexander, C. R., Smirnova, T. G., et al. (2016). A North American hourly assimilation and model forecast cycle: The rapid refresh. *Monthly Weather Review*, 144(4), 1669–1694. <https://doi.org/10.1175/MWR-D-15-0242.1>
- Benoit, R., Côté, J., & Mailhot, J. (1989). Inclusion of a TKE boundary layer parameterization in the Canadian regional finite-element model. *Monthly Weather Review*, 117(8), 1726–1750. [https://doi.org/10.1175/1520-0493\(1989\)117<1726:IOATBL>2.0.CO;2](https://doi.org/10.1175/1520-0493(1989)117<1726:IOATBL>2.0.CO;2)
- Blahak, U. (2016). RADAR\_MIE\_LM and RADAR\_MIELIB—Calculation of radar reflectivity from model output. In *COSMO technical report 28, consortium for small scale modeling (COSMO)*. Retrieved from <http://www.cosmo-model.org/content/model/documentation/techReports/cosmo/docs/techReport28.pdf>
- Bohren, C., & Huffman, D. (1983). *Absorption and scattering of light by small particles*, John Wiley. (p. 530). <https://doi.org/10.1002/9783527618156>
- Bourguin, P. (2000). A method to determine precipitation types. *Weather and Forecasting*, 15(5), 583–592. [https://doi.org/10.1175/1520-0434\(2000\)015<0583:AMTDPT>2.0.CO;2](https://doi.org/10.1175/1520-0434(2000)015<0583:AMTDPT>2.0.CO;2)
- Brown, P. R., & Francis, P. N. (1995). Improved measurements of the ice water content in cirrus using a total-water probe. *Journal of Atmospheric and Oceanic Technology*, 12(2), 410–414. [https://doi.org/10.1175/1520-0426\(1995\)012<0410:IMOTIW>2.0.CO;2](https://doi.org/10.1175/1520-0426(1995)012<0410:IMOTIW>2.0.CO;2)
- Bryan, G. H., Knievel, J. C., & Parker, M. D. (2006). A multimodel assessment of RKW theory's relevance to squall-line characteristics. *Monthly Weather Review*, 134(10), 2772–2792. <https://doi.org/10.1175/MWR3226>
- Cao, Q., Zhang, S., Lei, G., & Zhang, Y. (2022). Impact of different double-moment microphysical schemes on simulations of a bow-shaped squall line in East China. *Atmosphere*, 13(5), 667. <https://doi.org/10.3390/atmos13050667>
- Caron, J.-F., Jacques, D., Paquin-Ricard, D., Faucher, M., Milewski, T., & Verville, M. (2021). *High resolution deterministic prediction system—national domain (HRDPS-NAT). Update from version 5.2.0 to version 6.0.0* (p. 45). Technical Note, Canadian Meteorological Centre.
- Caron, J.-F., Milewski, T., Buehner, M., Fillion, L., MReszka, M., Macpherson, S., & St-James, J. (2015). Implementation of deterministic weather forecast systems based on ensemble-variational data assimilation at Environment Canada. Part II: The regional system. *Monthly Weather Review*, 143(7), 2560–2580. <https://doi.org/10.1175/MWR-D-14-00353.1>
- Cholette, M., Morrison, H., Milbrandt, J. A., & Thériault, J. M. (2019). Parameterization of the bulk liquid fraction on mixed-phase particles in the predicted particle properties (P3) scheme: Description and idealized simulations. *Journal of the Atmospheric Sciences*, 76(2), 561–582. <https://doi.org/10.1175/JAS-D-18-0278.1>
- Cholette, M., Thériault, J. M., Milbrandt, J. A., & Morrison, H. (2020). Impacts of predicting the liquid fraction of mixed-phase particles on the simulation of an extreme freezing rain event: The 1998 North American ice storm. *Monthly Weather Review*, 148(9), 3799–3823. <https://doi.org/10.1175/MWR-D-20-0026.1>
- Côté, J., Gravel, S., Méthot, A., Patoine, A., Roch, M., & Staniforth, A. (1998). The operational CMC-MRB global environmental multiscale (GEM) model. Part I: Design considerations and formulation. *Monthly Weather Review*, 126(6), 1373–1395. [https://doi.org/10.1175/1520-043\(1998\)126<1373:TOCMGE>2.0.CO;2](https://doi.org/10.1175/1520-043(1998)126<1373:TOCMGE>2.0.CO;2)
- Dawson, D. T., II, Mansell, E. R., Jung, Y., Wicker, L. J., Kumjian, M. R., & Xue, M. (2014). Low-level ZDR signatures in supercell forward flanks: The role of size sorting and melting of hail. *Journal of the Atmospheric Sciences*, 71(1), 276–299. <https://doi.org/10.1175/JAS-D-13-0118.1>
- Dawson, D. T., Xue, M., Milbrandt, J. A., & Yau, M. K. (2010). Comparison of evaporation and cold pool development between single-moment and multimoment bulk microphysics schemes in idealized simulations of tornadic thunderstorms. *Monthly Weather Review*, 138(4), 1152–1171. <https://doi.org/10.1175/2009MWR2956.1>
- Delage, Y. (1988a). A parameterization of the stable atmospheric boundary layer. *Boundary-Layer Meteorology*, 43(4), 365–381. <https://doi.org/10.1007/BF00121713>
- Delage, Y. (1988b). The position of the lowest levels in the boundary layer of atmospheric circulation models. *Atmosphere-Ocean*, 26(3), 329–340. <https://doi.org/10.1080/07055900.1988.9649307>
- Dietlicher, R., Neubauer, D., & Lohmann, U. (2018). Prognostic parameterization of cloud ice with a single category in the aerosol-climate model ECHAM (v6. 3.0)-HAM (v2. 3). *Geoscientific Model Development*, 11(4), 1557–1576. <https://doi.org/10.5194/gmd-11-1557-2018>
- Du, J. (2011). NCEP/EMC 4KM gridded data (GRIB) stage IV data. Version 1.0 [Dataset]. UCAR/NCAR – Earth Observing Laboratory. <https://doi.org/10.5065/D6PG1QDD>
- Fabry, F. (2015). *Radar meteorology principles and practice* (1st ed., p. 256). Cambridge University Press. <https://doi.org/10.1017/CBO9781107707405>
- Fabry, F., & Szyrmer, W. (1999). Modeling of the melting layer. Part II: Electromagnetic. *Journal of the Atmospheric Sciences*, 56(20), 3593–3600. [https://doi.org/10.1175/1520-0469\(1999\)056<3593:MOTMLP>2.0.CO;2](https://doi.org/10.1175/1520-0469(1999)056<3593:MOTMLP>2.0.CO;2)
- Fabry, F., & Zawadzki, I. (1995). Long-term radar observations of the melting layer of precipitation and their interpretation. *Journal of the Atmospheric Sciences*, 52(7), 838–851. [https://doi.org/10.1175/1520-0469\(1995\)052<0838:LTROOT>2.0.CO;2](https://doi.org/10.1175/1520-0469(1995)052<0838:LTROOT>2.0.CO;2)
- Fan, J., Han, B., Varble, A., Morrison, H., North, K., Kollias, P., et al. (2017). Cloud-resolving model intercomparison of an MC3E squall line case: Part I—Convective updrafts. *Journal of Geophysical Research: Atmospheres*, 122(17), 9351–9378. <https://doi.org/10.1002/2017JD026622>
- Ferrier, S. B. (1994). A double-moment multiple-phase four-class bulk ice scheme. Part I: Description. *Journal of the Atmospheric Sciences*, 51(2), 249–280. [https://doi.org/10.1175/1520-0469\(1994\)051<0249:ADMMPF>2.0.CO;2](https://doi.org/10.1175/1520-0469(1994)051<0249:ADMMPF>2.0.CO;2)
- Forbes, R. I. C. H. A. R. D., Tsonevsky, I. V. A. N., Hewson, T., & Leutbecher, M. A. R. T. I. N. (2014). Towards predicting high-impact freezing rain events. *ECMWF Newsletter*, 141, 15–21.
- Frick, C., Seifert, A., & Wernli, H. (2013). A bulk parametrization of melting snowflakes with explicit liquid water fraction for the COSMO model. *Geoscientific Model Development*, 6(6), 1925–1939. <https://doi.org/10.5194/gmd-6-1925-2013>
- Fujiyoshi, Y. (1986). Melting snowflakes. *Journal of the Atmospheric Sciences*, 43(3), 307–311. [https://doi.org/10.1175/1520-0469\(1986\)043<0307:MS>2.0.CO;2](https://doi.org/10.1175/1520-0469(1986)043<0307:MS>2.0.CO;2)
- Garnett, J. M. (1904). XII. Colours in metal glasses and in metallic films. *Philosophical Transactions of the Royal Society of London - Series A: Containing Papers of a Mathematical or Physical Character*, 203(359–371), 385–420. <https://doi.org/10.1098/rsta.1904.0024>
- Gascón, E., Hewson, T., & Haider, T. (2018). Improving predictions of precipitation type at the surface: Description and verification of two new products from the ECMWF ensemble. *Weather and Forecasting*, 33(1), 89–108. <https://doi.org/10.1175/WAF-D-17-0114.1>

- Girard, C., Plante, A., Desgagné, M., McTaggart-Cowan, R., Côté, J., Charron, M., et al. (2014). Staggered vertical discretization of the Canadian environmental multiscale (GEM) model using a coordinate of the log-hydrostatic-pressure type. *Monthly Weather Review*, 142(3), 1183–1196. <https://doi.org/10.1175/MWR-D-13-00255.1>
- Guo, H., Ming, Y., Fan, S., Zhou, L., Harris, L., & Zhao, M. (2021). Two-moment bulk cloud microphysics with prognostic precipitation in GFDL's atmosphere model AM4.0: Configuration and performance. *Journal of Advances in Modeling Earth Systems*, 13(6), e2020MS002453. <https://doi.org/10.1029/2020MS002453>
- Han, B., Fan, J., Varble, A., Morrison, H., Williams, C. R., Chen, B., et al. (2019). Cloud-resolving model intercomparison of an MC3E squall line case: Part II. Stratiform precipitation properties. *Journal of Geophysical Research: Atmospheres*, 124(2), 1090–1117. <https://doi.org/10.1029/2018JD029596>
- Hashino, T., & Tripoli, G. J. (2007). The spectral ice habit prediction system (SHIPS). Part I: Model description and simulation of the vapor deposition process. *Journal of the Atmospheric Sciences*, 64(7), 2210–2237. <https://doi.org/10.1175/JAS3963.1>
- Hersbach, H., Bell, B., Berrisford, P., Hirahara, S., Horányi, A., Muñoz-Sabater, J., et al. (2020). The ERA5 global reanalysis [Dataset]. Quarterly Journal of the Royal Meteorological Society, 146, 1999–2049. <https://doi.org/10.1002/qj.3803>
- Heymsfield, A. J. (2003). Properties of tropical and midlatitude ice cloud particle ensembles. Part I: Median mass diameters and terminal velocities. *Journal of the Atmospheric Sciences*, 60(21), 2573–2591. [https://doi.org/10.1175/1520-0469\(2003\)060<2573:POTAMI>2.0.CO;2](https://doi.org/10.1175/1520-0469(2003)060<2573:POTAMI>2.0.CO;2)
- Hindmarsh, J. P., Russell, A. B., & Chen, X. D. (2003). Experimental and numerical analysis of the temperature transition of a suspended freezing water droplet. *International Journal of Heat and Mass Transfer*, 46(7), 1199–1213. [https://doi.org/10.1016/S0017-9310\(02\)00399-X](https://doi.org/10.1016/S0017-9310(02)00399-X)
- Hogan, R. J., Tian, L., Brown, P. R., Westbrook, C. D., Heymsfield, A. J., & Eastment, J. D. (2012). Radar scattering from ice aggregates using the horizontally aligned oblate spheroid approximation. *Journal of Applied Meteorology and Climatology*, 51(3), 655–671. <https://doi.org/10.1175/JAMC-D-11-074.1>
- Houze, R. A., Jr. (2018). 100 years of research on mesoscale convective systems. *Meteorological Monographs*, 59, 17.1–17.54. <https://doi.org/10.1175/AMSMONOGRAPH-D-18-0001.1>
- Huang, Y., Wu, W., McFarquhar, G. M., Wang, X., Morrison, H., Ryzhkov, A., et al. (2021). Microphysical processes producing high ice water contents (HIWCs) in tropical convective clouds during the HAIC-HIWC field campaign: Evaluation of simulations using bulk microphysical schemes. *Atmospheric Chemistry and Physics*, 21(9), 6919–6944. <https://doi.org/10.5194/acp-21-6919-2021>
- Ikeda, K., Steiner, M., & Thompson, G. (2017). Examination of mixed-phase precipitation forecasts from the high-resolution rapid refresh model using surface observations and sounding data. *Weather and Forecasting*, 32(3), 949–967. <https://doi.org/10.1175/WAF-D-16-0171.1>
- Jacques, D., & Michelson, D. (2022). Latent heat nudging in the Canadian High resolution (2.5 km) regional deterministic prediction system. *Monthly Weather Review*, 150(9), 2299–2315. <https://doi.org/10.1175/MWR-D-22-0028.1>
- Jacques, D., Michelson, D., Caron, J. F., & Fillion, L. (2018). Latent heat nudging in the Canadian regional deterministic prediction system. *Monthly Weather Review*, 146(12), 3995–4014. <https://doi.org/10.1175/MWR-D-18-0118.1>
- Jensen, A. A., Harrington, J. Y., & Morrison, H. (2018). Microphysical characteristics of squall-line stratiform precipitation and transition zones simulated using an ice particle property-evolving model. *Monthly Weather Review*, 146(3), 723–743. <https://doi.org/10.1175/MWR-D-17-0215.1>
- Jensen, A. A., Harrington, J. Y., Morrison, H., & Milbrandt, J. A. (2017). Predicting ice shape evolution in a bulk microphysics model. *Journal of the Atmospheric Sciences*, 74(6), 2081–2104. <https://doi.org/10.1175/JAS-D-16-0350.1>
- Johnson, M., Jung, Y., Milbrandt, J. A., Morrison, H., & Xue, M. (2019). Effects of the representation of rimed ice in bulk microphysics schemes on polarimetric signatures. *Monthly Weather Review*, 147(10), 3785–3810. <https://doi.org/10.1175/MWR-D-18-0398.1>
- Jouan, C., & Milbrandt, J. A. (2019). The importance of the ice-phase microphysics parameterization for simulating the effects of changes to CCN concentrations in deep convection. *Journal of the Atmospheric Sciences*, 76(6), 1727–1752. <https://doi.org/10.1175/JAS-D-18-0168.1>
- Jouan, C., Milbrandt, J. A., Vaillancourt, P. A., Chosson, F., & Morrison, H. (2020). Adaptation of the Predicted Particles Properties (P3) microphysics scheme for large-scale numerical weather prediction. *Weather and Forecasting*, 35(6), 2541–2565. <https://doi.org/10.1175/WAF-D-20-0111.1>
- Kain, J. S., & Fritsch, J. M. (1990). A one-dimensional entraining/detraining plume model and its application in convective parameterization. *Journal of the Atmospheric Sciences*, 47(23), 2784–2802. [https://doi.org/10.1175/1520-0469\(1990\)047<2784:AODEPM>2.0.CO;2](https://doi.org/10.1175/1520-0469(1990)047<2784:AODEPM>2.0.CO;2)
- Kain, J. S., & Fritsch, J. M. (1993). Convective parameterization for mesoscale models: The Kain-Fritsch scheme. In K. A. Emanuel & D. J. Raymond (Eds.), *The representation of Cumulus convection in numerical models. Meteorological monographs*. American Meteorological Society. [https://doi.org/10.1007/978-1-935704-13-3\\_16](https://doi.org/10.1007/978-1-935704-13-3_16)
- Korolev, A., McFarquhar, G., Field, P. R., Franklin, C., Lawson, P., Wang, Z., et al. (2017). Mixed-phase clouds: Progress and challenges. *Meteorological Monographs*, 58, 5–1. <https://doi.org/10.1175/AMSMONOGRAPH-D-17-0001.1>
- Kringlebotn Nygaard, B. E., Ágústsson, H., & Somfalvi-Tóth, K. (2013). Modeling wet snow accretion on power lines: Improvements to previous methods using 50 years of observations. *Journal of Applied Meteorology and Climatology*, 52(10), 2189–2203. <https://doi.org/10.1175/JAMC-D-12-0332.1>
- Li, J., & Barker, H. W. (2005). A radiation algorithm with correlated-k distribution. Part I: Local thermal equilibrium. *Journal of the Atmospheric Sciences*, 62(2), 286–309. <https://doi.org/10.1175/JAS-3396.1>
- Li, Z., Liu, Q., Chen, X., Ma, Z., Chen, J., & Jiang, Y. (2021). Simulation study of a squall line hailstorm using high-resolution GRAPES-Meso with a modified double-moment microphysics scheme. *Geoscientific Model Development Discussions*, 1–24. <https://doi.org/10.5194/gmd-2020-439>
- Li, Z., Zuidema, P., Zhu, P., & Morrison, H. (2015). The sensitivity of simulated shallow cumulus convection and cold pools to microphysics. *Journal of the Atmospheric Sciences*, 72(9), 3340–3355. <https://doi.org/10.1175/AMSMONOGRAPH-D-17-0001.1>
- Liu, C., Moncrieff, M. W., & Zipser, E. J. (1997). Dynamical influence of microphysics in tropical squall lines: A numerical study. *Monthly Weather Review*, 125(9), 2193–2210. [https://doi.org/10.1175/1520-0493\(1997\)125<2193:DIOMIT>2.0.CO;2](https://doi.org/10.1175/1520-0493(1997)125<2193:DIOMIT>2.0.CO;2)
- Loftus, A. M., Cotton, W. R., & Carrión, G. G. (2014). A triple-moment hail bulk microphysics scheme. Part I: Description and initial evaluation. *Atmospheric Research*, 149, 35–57. <https://doi.org/10.1016/j.atmosres.2014.05.013>
- Luo, L., Xue, M., Zhu, K., & Zhou, B. (2018). Explicit prediction of hail in a long-lasting multicellular convective system in eastern China using multimoment microphysics schemes. *Journal of the Atmospheric Sciences*, 75(9), 3115–3137. <https://doi.org/10.1175/JAS-D-17-0302.1>
- Luo, T., Xie, Y., Wang, R., & Yu, X. (2022). An analytic solution to precipitation attenuation expression with spaceborne synthetic aperture radar based on volterra integral equation. *Remote Sensing*, 14(2), 357. <https://doi.org/10.3390/rs14020357>
- Luo, Y., & Chen, Y. (2015). Investigation of the predictability and physical mechanisms of an extreme rainfall-producing mesoscale convective system along the Meiyu front in East China: An ensemble approach. *Journal of Geophysical Research: Atmospheres*, 120(20), 10–593. <https://doi.org/10.1002/2015JD023584>

- Mansell, E. R., Dawson, D. T., II., & Straka, J. M. (2020). Bin-emulating hail melting in three-moment bulk microphysics. *Journal of the Atmospheric Sciences*, 77(10), 3361–3385. <https://doi.org/10.1175/JAS-D-19-0268.1>
- McTaggart-Cowan, R., Vaillancourt, P. A., Zadra, A., Chamberland, S., Charron, M., Corvec, S., et al. (2019). Modernization of atmospheric physics parameterization in Canadian NWP. *Journal of Advances in Modeling Earth Systems*, 11(11), 3593–3635. <https://doi.org/10.1029/2019MS001781>
- Michelson, D., Henja, A., Ernes, S., Haase, G., Koistinen, J., Ośrońska, K., et al. (2018). BALTRAD advanced weather radar networking [Dataset]. Journal of Open Research Software, 6, 12. <https://doi.org/10.5334/jors.193>
- Milbrandt, J. A., Bélair, S., Faucher, M., Vallée, M., Carrera, M. L., & Glazer, A. (2016). The pan-Canadian high resolution (2.5 km) deterministic prediction system. *Weather and Forecasting*, 31(6), 1791–1816. <https://doi.org/10.1175/WAF-D-16-0035.1>
- Milbrandt, J. A., Glazer, A., & Jacob, D. (2012). Predicting the snow-to-liquid ratio of surface precipitation using a bulk microphysics scheme. *Monthly Weather Review*, 140(8), 2461–2476. <https://doi.org/10.1175/MWR-D-11-00286.1>
- Milbrandt, J. A., Leroyer, S., Paquin-Ricard, D., Faucher, M., Zhang, S., & Jouan, C. (2018). *High resolution deterministic prediction system HRDPS. Update from version 4.4.0 to version 5.0.0* (p. 57). Technical Note, Canadian Meteorological Centre.
- Milbrandt, J. A., & Morrison, H. (2016). Parameterization of cloud microphysics based on the prediction of bulk ice particle properties. Part III: Introduction of multiple free categories. *Journal of the Atmospheric Sciences*, 73(3), 975–995. <https://doi.org/10.1175/JAS-D-15-0204.1>
- Milbrandt, J. A., Morrison, H., Dawson, D. T., II., & Paukert, M. (2021). A triple-moment representation of ice in the Predicted Particle Properties (P3) microphysics scheme. *Journal of the Atmospheric Sciences*, 78(2), 439–458. <https://doi.org/10.1175/JAS-D-20-0084.1>
- Milbrandt, J. A., & Yau, M. K. (2005). A multimoment bulk microphysics parameterization. Part I: Analysis of the role of the spectral shape parameter. *Journal of the Atmospheric Sciences*, 62(9), 3051–3064. <https://doi.org/10.1175/JAS3534.1>
- Morrison, H., Jensen, A. A., Harrington, J. Y., & Milbrandt, J. A. (2016). Advection of coupled hydrometeor quantities in bulk cloud microphysics schemes. *Monthly Weather Review*, 144(8), 2809–2829. <https://doi.org/10.1175/MWR-D-15-0368.1>
- Morrison, H., & Milbrandt, J. A. (2015). Parameterization of cloud microphysics based on the prediction of bulk ice particle properties. Part I: Scheme description and idealized tests. *Journal of the Atmospheric Sciences*, 72(1), 287–311. <https://doi.org/10.1175/JAS-D-14-0065.1>
- Morrison, H., Milbrandt, J. A., Bryan, G. H., Ikeda, K., Tessendorf, S. A., & Thompson, G. (2015). Parameterization of cloud microphysics based on the prediction of bulk ice particle properties. Part II: Case study comparisons with observations and other schemes. *Journal of the Atmospheric Sciences*, 72(1), 312–339. <https://doi.org/10.1175/JAS-D-14-0066.1>
- Morrison, H., Thompson, G., & Tatarkiiv, V. (2009). Impact of cloud microphysics on the development of trailing stratiform precipitation in a simulated squall line: Comparison of one-and two-moment schemes. *Monthly Weather Review*, 137(3), 991–1007. <https://doi.org/10.1175/2008MWR2556.1>
- Morrison, H., van Lier-Walqui, M., Fridlind, A. M., Grabowski, W. W., Harrington, J. Y., Hoose, C., et al. (2020). Confronting the challenge of modeling cloud and precipitation microphysics. *Journal of Advances in Modeling Earth Systems*, 12(8), e2019MS001689. <https://doi.org/10.1029/2019MS001689>
- Musil, D. J. (1970). Computer modeling of hailstone growth in feeder clouds. *Journal of the Atmospheric Sciences*, 27(3), 474–482. [https://doi.org/10.1175/1520-0469\(1970\)027<0474:CMOHGI>2.0.CO;2](https://doi.org/10.1175/1520-0469(1970)027<0474:CMOHGI>2.0.CO;2)
- Nagumo, N., Adachi, A., & Yamauchi, H. (2019). Geometrical properties of hydrometeors during the refreezing process and their effects on dual-polarized radar signals. *Monthly Weather Review*, 147(5), 1753–1768. <https://doi.org/10.1175/MWR-D-18-0278.1>
- Parker, M. D., & Johnson, R. H. (2000). Organizational modes of midlatitude mesoscale convective systems. *Monthly Weather Review*, 128(10), 3413–3436. [https://doi.org/10.1175/1520-0493\(2001\)129<3413:OMOMMC>2.0.CO;2](https://doi.org/10.1175/1520-0493(2001)129<3413:OMOMMC>2.0.CO;2)
- Paukert, M., Fan, J., Rasch, P. J., Morrison, H., Milbrandt, J. A., Shpund, J., & Khain, A. (2019). Three-moment representation of rain in a bulk microphysics model. *Journal of Advances in Modeling Earth Systems*, 11(1), 257–277. <https://doi.org/10.1029/2018MS001512>
- Phillips, V. T. J., Khain, A., Benmoshe, N., & Ilotoviz, E. (2014). Theory of time-dependent freezing. Part I: Description of scheme for wet growth of hail. *Journal of the Atmospheric Sciences*, 71(12), 4527–4557. <https://doi.org/10.1175/JAS-D-13-0375.1>
- Pi, C. J., & Chen, J. P. (2021). Integrated cloud macro-and micro-physics schemes with kinetic treatment of condensation processes for global models. *Atmospheric Research*, 261, 105745. <https://doi.org/10.1016/j.atmosres.2021.105745>
- Pruppacher, H. R., & Klett, J. D. (1997). *Microphysics of clouds and precipitation* (p. 954). Springer.
- Rasmussen, R., & Pruppacher, H. R. (1982). A wind tunnel and theoretical study of the melting behavior of atmospheric ice particles. I: A wind tunnel study of frozen drops of radius < 500 μm. *Journal of the Atmospheric Sciences*, 39(1), 152–158. [https://doi.org/10.1175/1520-0469\(1982\)039<0152:AWTATS>2.0.CO;2](https://doi.org/10.1175/1520-0469(1982)039<0152:AWTATS>2.0.CO;2)
- Rasmussen, R. M., Levizzani, V., & Pruppacher, H. R. (1984a). A wind tunnel and theoretical study of the melting behavior of atmospheric ice particles. II: A theoretical study for frozen drops of radius < 500 μm. *Journal of the Atmospheric Sciences*, 41(3), 374–380. [https://doi.org/10.1175/1520-0469\(1984\)041<0374:AWTATS>2.0.CO;2](https://doi.org/10.1175/1520-0469(1984)041<0374:AWTATS>2.0.CO;2)
- Rasmussen, R. M., Levizzani, V., & Pruppacher, H. R. (1984b). A wind tunnel and theoretical study on the melting behavior of atmospheric ice particles: III. Experiment and theory for spherical ice particles of radius > 500 μm. *Journal of the Atmospheric Sciences*, 41(3), 381–388. [https://doi.org/10.1175/1520-0469\(1984\)041<0381:AWTATS>2.0.CO;2](https://doi.org/10.1175/1520-0469(1984)041<0381:AWTATS>2.0.CO;2)
- Reeves, H. D., Ryzhkov, A. V., & Krause, J. (2016). Discrimination between winter precipitation types based on spectral-bin microphysical modeling. *Journal of Applied Meteorology and Climatology*, 55(8), 1747–1761. <https://doi.org/10.1175/JAMC-D-16-0044.1>
- Ryzhkov, A. V., Snyder, J., Carlin, J. T., Khain, A., & Pinsky, M. (2020). What polarimetric weather radars offer to cloud modelers: Forward radar operators and microphysical/thermodynamic retrievals. *Atmosphere*, 11(4), 362. <https://doi.org/10.3390/atmos11040362>
- Shan, Y., Wilcox, E. M., Gao, L., Lin, L., Mitchell, D. L., Yin, Y., et al. (2020). Evaluating errors in gamma-function representations of the raindrop size distribution: A method for determining the optimal parameter set for use in bulk microphysics schemes. *Journal of the Atmospheric Sciences*, 77(2), 513–529. <https://doi.org/10.1175/JAS-D-18-0259.1>
- Shrestha, P., Mendrok, J., Pejcic, V., Trömel, S., Blahak, U., & Carlin, J. T. (2022). Evaluation of the COSMO model (v5.1) in polarimetric radar space–impact of uncertainties in model microphysics, retrievals and forward operators. *Geoscientific Model Development*, 15(1), 291–313. <https://doi.org/10.5194/gmd-15-291-2022>
- Skamarock, W. C., & Klemp, J. B. (2008). A time-split nonhydrostatic atmospheric model for weather research and forecasting applications. *Journal of Computational Physics*, 227(7), 3465–3485. <https://doi.org/10.1016/j.jcp.2007.01.037>
- Skamarock, W. C., Klemp, J. B., Dudhia, J., Gill, D. O., Liu, Z., Berner, J., et al. (2019). A Description of the Advanced Research WRF Version 4 (p. 145). NCAR Tech. Note NCAR/TN-556+STR. <https://doi.org/10.5056/1dfh-6p97>
- Sundqvist, H., Berge, E., & Kristjánsson, J. E. (1989). Condensation and cloud parameterization studies with a mesoscale numerical weather prediction model. *Monthly Weather Review*, 117(8), 1641–1657. [https://doi.org/10.1175/1520-0493\(1989\)117<1641:CAPSW>2.0.CO;2](https://doi.org/10.1175/1520-0493(1989)117<1641:CAPSW>2.0.CO;2)
- Tao, W. K., Scala, J. R., Ferrier, B., & Simpson, J. (1995). The effect of melting processes on the development of a tropical and a midlatitude squall line. *Journal of the Atmospheric Sciences*, 52(11), 1934–1948. [https://doi.org/10.1175/1520-0469\(1995\)052<1934:TEOMPO>2.0.CO;2](https://doi.org/10.1175/1520-0469(1995)052<1934:TEOMPO>2.0.CO;2)

- Thompson, G. (2019). High resolution numerical weather model forecasts of icing at the ground and in the air. In *Proceedings International Workshop on atmospheric icing of structures, Reykjavík, Iceland* (p. 6). IWAIS. Retrieved from [https://iwais2019.is/images/Papers/042\\_iwais\\_thompson.pdf](https://iwais2019.is/images/Papers/042_iwais_thompson.pdf)
- Tobin, D. M., & Kumjian, M. R. (2017). Polarimetric radar and surface-based precipitation-type observations of ice pellet to freezing rain transitions. *Weather and Forecasting*, 32(6), 2065–2082. <https://doi.org/10.1175/WAF-D-17-0054.1>
- Tsai, T. C., & Chen, J. P. (2020). Multimoment ice bulk microphysics scheme with consideration for particle shape and apparent density. Part I: Methodology and idealized simulation. *Journal of the Atmospheric Sciences*, 77(5), 1821–1850. <https://doi.org/10.1175/JAS-D-19-0125.1>
- Vié, B., Pinty, J. P., Berthet, S., & Leriche, M. (2016). LIMA (v1.0): A quasi two-moment microphysical scheme driven by a multimodal population of cloud condensation and ice freezing nuclei. *Geoscientific Model Development*, 9(2), 567–586. <https://doi.org/10.5194/gmd-9-567-2016>
- Walko, R. L., Cotton, W. R., Feingold, G., & Stevens, B. (2000). Efficient computation of vapor and heat diffusion between hydrometeors in a numerical model. *Atmospheric Research*, 53(1–3), 171–183. [https://doi.org/10.1016/S0169-8095\(99\)00044-7](https://doi.org/10.1016/S0169-8095(99)00044-7)
- Wang, H. L., Sun, J., Guo, Y. R., Huang, X. Y., & Sugimoto, S. (2011). Radar reflectivity assimilation with the updated WRFDA-4DVAR system. In *91st American meteorological society annual meeting* (pp. 23–27).
- Wang, J., Fan, J., Feng, Z., Zhang, K., Roesler, E., Hillman, B., et al. (2021). Impact of a new cloud microphysics parameterization on the simulations of mesoscale convective systems in E3SM. *Journal of Advances in Modeling Earth Systems*, 13(11), e2021MS002628. <https://doi.org/10.1029/2021MS002628>
- Weisman, M. L., Skamarock, W. C., & Klemp, J. B. (1997). The resolution dependence of explicitly modeled convective systems. *Monthly Weather Review*, 125(4), 527–548. [https://doi.org/10.1175/1520-0493\(1997\)125<0527:TRDOIEM>2.0.CO;2](https://doi.org/10.1175/1520-0493(1997)125<0527:TRDOIEM>2.0.CO;2)
- Wen, J., Zhao, K., Huang, H., Zhou, B., Yang, Z., Chen, G., et al. (2017). Evolution of microphysical structure of a subtropical squall line observed by a polarimetric radar and a disdrometer during OPACC in Eastern China. *Journal of Geophysical Research: Atmospheres*, 122(15), 8033–8050. <https://doi.org/10.1002/2016JD026346>
- Wolfensberger, D., & Berne, A. (2018). From model to radar variables: A new forward polarimetric radar operator for COSMO. *Atmospheric Measurement Techniques*, 11(7), 3883–3916. <https://doi.org/10.5194/amt-11-3883-2018>
- Wu, D., Dong, X., Xi, B., Feng, Z., Kennedy, A., Mullendore, G., et al. (2013). Impacts of microphysical scheme on convective and stratiform characteristics in two high precipitation squall line events. *Journal of Geophysical Research: Atmospheres*, 118(19), 11–119. <https://doi.org/10.1002/jgrd.50798>
- Xu, M., Thompson, G., Adriaansen, D. R., & Landoit, S. D. (2019). On the value of time-lag-ensemble averaging to improve numerical model predictions of aircraft icing conditions. *Weather and Forecasting*, 34(3), 507–519. <https://doi.org/10.1175/WAF-D-18-0087.1>
- Zhang, J., Howard, K., Langston, C., Vasiloff, S., Kaney, B., Arthur, A., et al. (2011). National Mosaic and Multi-Sensor QPE (NMQ) system: Description, results, and future plans [Dataset]. Bulletin of the American Meteorological Society, 92, 1321–1338. <https://doi.org/10.1175/2011BAMS-D-11-00047.1>
- Zhao, X., Lin, Y., Luo, Y., Qian, Q., Liu, X., Liu, X., & Colle, B. A. (2021). A double-moment SBV-YLIN cloud microphysics scheme and its impact on a squall line simulation. *Journal of Advances in Modeling Earth Systems*, 13(11), e2021MS002545. <https://doi.org/10.1029/2021MS002545>